Evaluation and Improvement of Photovoltaic Power Systems
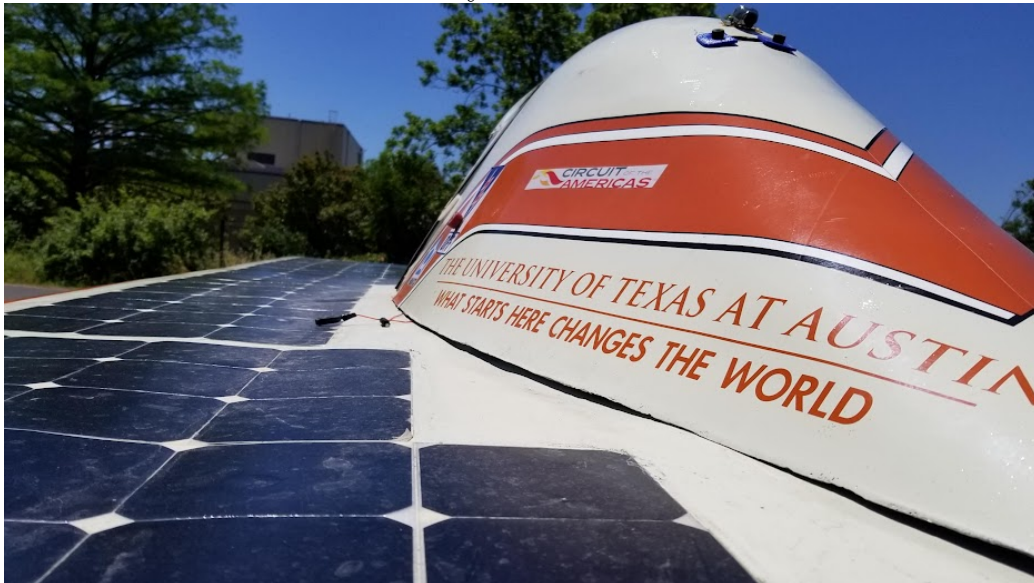
The University of Texas at Austin

Matthew Junkit Yu

26 December 2022

Contents

List of Figures

List of Tables

Chapter 1

Introduction

In order to reach net zero emissions targets set by the United Nations (UN) at the 2015 Paris Agreement [26] before 2050, the International Energy Association (IEA) estimates that nearly 630 Gigawatts (GW) [24] of photovoltaic (PV) energy generation capacity need to be added annually by 2030. As of 2022, we observed that at least 175 GW were installed in 2021 [19] [18], a 22% year over year growth. With large policy and geopolitical tailwinds behind major economies like the United States and Europe, solar is expected to be one of the, if not the major driver of new energy generation within the next two decades.

However, in order to achieve this target generation capacity in a sustainable way, engineers and PV designers need to maximize the electrical efficiency of the overall power system, as opposed to just improving the solar cell efficiency. According to the U.S. Energy Information Administration (EIA) [31], the capacity factor of PVs as an energy source in the United States reached a monthly maximum of 33.4% in June of 2022; *capacity factor* is defined by the EIA as a measure of the generated output by the electric generator versus the maximum possible output. It is clear that system inefficiencies in PV generation provide large constraints, and optimistically, equally large opportunities, in allowing us to increase our pace towards reaching net zero carbon emissions by 2050.

This thesis takes a holistic evaluation of the PV power generation system in a unique use case that necessitates maximizing the capacity factor: solar powered vehicles. We evaluate the modeling, creation, and optimization of a solar powered vehicle for the University of Texas at Austin's Longhorn Racing Solar (LHRs) team, and attempt to identify and address inefficiencies and

bottlenecks whose improvements will help the larger PV industry as a whole.

In particular, this thesis will focus on three important and active areas of development within the PV field: solar array modeling and prediction, solar cell binning processes and heuristics, and maximum power point tracking (MPPT) algorithms. In each of these areas, we look at the state of the art techniques, propose novel ideas to improve our understanding of the system and its inefficiencies, and see if we can translate it lateral applications like rooftop solar or industrial PV. Note that in this thesis we refer to photovoltaics and solar without distinction.

The second area of development may be more generalized then this.

In the first major chapter, **Modeling Photovoltaics**, this thesis discusses how can solar cells can be modeled at various abstraction layers, from idealized cells at standard conditions using the 3-parameter model to non-idealized cells that incorporate parasitic resistances using the 7-parameter model. These solar cell models are then evaluated against a dataset of several hundred solar cell I-V and power-voltage (P-V) curves generated from our custom testing setup to see how well the model fits real cells at different conditions. We build upon these models to form larger units of PVs, such as solar modules and solar arrays, which may consist of strings of cells in series with bypass diodes across them, among other configurations. Some important topics that are explored using these multi-cell models include PV mismatch and bypass activation. Insights from these topics lead to heuristics that are proposed in the next chapter, **Optimizing Photovoltaics**.

The second major chapter, **Optimizing Photovoltaics**, takes the aforementioned models and dataset created to propose a process to bin, match, and combine solar cells and modules, with the end goal of maximizing the performance of the solar array that will be attached to the solar vehicle. In this chapter, we propose design criteria, heuristics, and methodologies to generate designs for the solar vehicle that fit the unique constraints of the application, which center around the dynamism of the system as it moves in transit across the real world.

In the third and final major chapter, **Optimizing Photovoltaic Systems**, this thesis investigates the operation of the PV system in the context of the solar vehicle. We observe the energy conversion process from incident light on the solar array to electricity captured by the battery protection system (BPS) and present a PV system simulator and a suite of MPPT algorithms to minimize energy losses from the aforementioned conversion process. We demonstrate custom hardware developed by the LHRs team and evaluate in real world settings a select set of MPPT algorithms. We compare

these results with existing research and our digital twin model of the solar vehicle, and finally discuss conclusions from the three chapters that can be translatable to the wider PV industry.

Along with these three major chapters, we also provide a large set of appendices corresponding to the development of the main body of work in this thesis. Among them include manufacturing procedures for testing, assembling, and laminating solar cells into solar modules, schematics and accompanying documentation for hardware that was used for characterizing and validating parts of the thesis, software diagrams with relevant open source software repositories developed by our team, and extra insights into the design of the LHRs' photovoltaic array that are not directly applicable to the major chapters, such as thermal models performed of the vehicle topshell that influenced our simulation models, among others.

Chapter 2

Modeling Photovoltaics

In this chapter, **Modeling Photovoltaics**, we systematically review the various types of abstractions in photovoltaics, starting from solar cells and ending with solar arrays.

We start by observing how solar cell models can have differing granularities in their composition and in how they address an array of internal qualities and external environs that influence real world performance. Alongside defining these models, we also propose modifications that may improve their accuracy and precision, and consider tradeoffs that may occur in nonnominal conditions. After defining these models, we then present an in-depth methodology for evaluating them; we construct a dataset of solar cell I-V curves characterized for use on the LHRs solar vehicle, then define techniques for extracting model parameters for each cell. We proceed to use those model parameters to predict their behavior in different conditions, and evaluate how they perform in terms of model accuracy and precision.

We select the 'best' set of solar cell models and use them as building blocks to build larger models, namely those for solar modules. These solar modules can take multiple shapes and sizes, and may exhibit reverse bias behavior in the event of photovoltaic mismatch, a phenomenon caused by nonuniform cells in series or in parallel. We also extend the module model by adding a bypass diode in antiparallel, and discussing how solar cell reverse bias behavior may drive their turn on conditions and mismatch mitigation effects. From these solar module models, we formulate a metric to measure mismatch, and propose suggestions and observations on how module size and cell characteristics may influence the total efficiency of the module. Insights developed in this section will later on become heuristics and algorithms for

optimizing module design in chapter 3. We extend the test methodology used for evaluating solar cells to solar modules, and validate whether the module models pass muster.

Finally, we take these solar module models and combine them together to form a cohesive solar array model. From this model, we observe how the individual module effects can generate a global I-V curve with local and global maxima, and discuss how this curve impacts the way the larger photovoltaic system interacts with solar arrays. We also perform array testing using the LHRs solar array, and compare a simulated version of the array test with real world data to determine a final, holistic evaluation of the models used.

2.1   Modeling Solar Cells

In this thesis, we will discuss three solar cell model abstractions:

- Three Parameter Solar Cell Model (Single Diode Model)

- Five Parameter Solar Cell Model (Complete Single Diode Model)

- Seven Parameter Solar Cell Model (Double Diode Model)

To restrain the breadth of this document, we'll focus on the aforementioned three models, since they are the most commonly cited and used abstractions. That is not to diminish the dozens, if not hundreds more types of solar cell models, like the three diode model proposed by Khanna et al [15], or the Bishop model with an avalanche breakdown component [27], or the Direct-Reverse Model (DRM) that utilizes antiparallel diode-resistor paths [27].

2.1.1   Three Parameter Solar Cell Model

The most basic model of a solar cell is the three parameter model, or single diode model, shown in Figure 2.1. It consists of a constant current source and a diode. The constant current source produces a photocurrent, or light generated current (I_{PV}) caused by photons of sufficient energy being absorbed into the surface of the solar cell and exciting charge carriers (generally in the form of electrons) to enter the circuit. The diode represents the various recombination processes that consume the generated current in the form of dark current, or diode current (I_D).
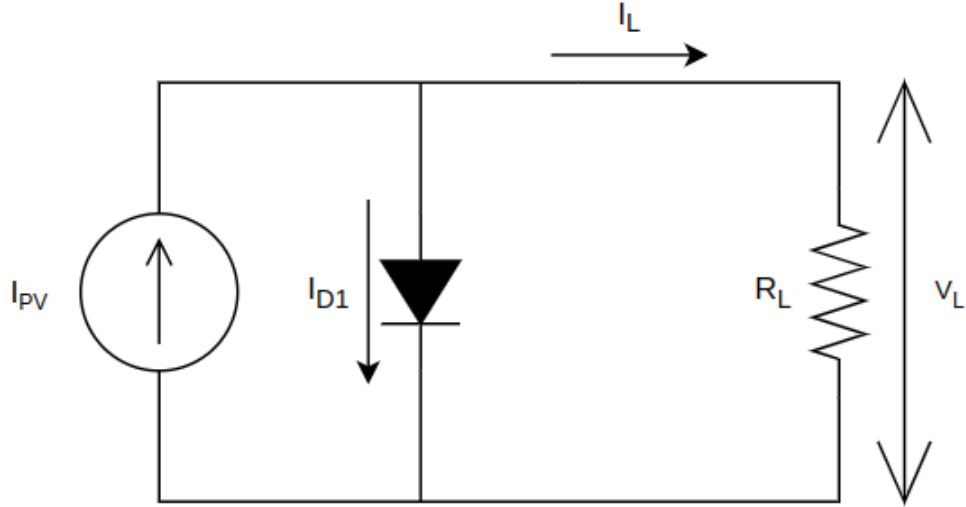
Figure 2.1: Three Parameter, or Single Diode Model of a Solar Cell

In this model, the three parameters consist of the following:

- photocurrent, or light generated current (I_{PV}),

- dark saturation current, or reverse saturation current (I_0),

- and an ideality factor (n).

The latter two are contained within the dark current term, and generally influence the shape of the predicted I-V curve, particularly around the knee-bend.

This model is juxtaposed from the five parameter model in that it does not incorporate cell losses in the form of series resistance (R_S) and shunt resistance (R_{SH}). It is assumed that in this model, the series resistance is zero (short circuit) and the shunt resistance is infinite (open circuit). Therefore, the five parameter model may also be called the complete single diode model.

We observe from Figure 2.1 that the load current (I_L) can be represented as a function of the photocurrent and the dark current (Equation 2.1).

$$I_L = I_{PV} - I_D \qquad\qquad \text{(A)} \quad (2.1)$$

In the following text, we break down each component into its constituent parts.

2.1.1.1 Photocurrent

$$I_{PV} = qA \int b_s(E) QE(E) dE \qquad \text{(A)} \quad (2.2)$$

On a fundamental level, we can define the photocurrent, or light generated current (I_{PV}) as a function of the photons incident upon the surface of the solar cell and the solar cell's spectral response. This is demonstrated in Equation 2.2. A bulleted, simplistic explanation of this equation is presented as follows:

- Incident light hits the solar cell over a given spectrum of energy levels (denoted either in eV or in nm) (see Figure 2.2).

- Incident light at each discrete energy level has an spectral photon flux density ($b_S(E)$), otherwise known as intensity.

- The solar cell has a given quantum efficiency ($QE(E)$) at each energy level that is the probability that an incident photon of energy (E) delivers one electron to the external circuit.

- Integrating the product of the photon flux density $b_S(E)$ and quantum efficiency $QE(E)$ (then multiplied by the electric charge constant (q) and the cell area (A)) provides the photocurrent (I_{PV}).

Solar cell manufacturers may provide a spectral response chart showing the quantum efficiency over the useful solar spectrum, as seen in Figure 2.2, but will generally just provide the short circuit current (I_{SC}) at standard test conditions (STC) (1000 Wm^{-2}, AM 1.5G, 25 C).

As it turns out, the photocurrent can generally be approximated as the short circuit current. We'll discuss in subsubsection 2.1.2.2 that Cubas et al. [5, 6] defines the photocurrent as a ratio of the series and shunt resistance in addition to the short circuit current. However, in most cases, the empirical value of short circuit current will not differ from Equation 2.3.

$$I_{PV} = I_{SC} \qquad \text{(A)} \quad (2.3)$$

2.1.1.2 Dark Current

The dark current, or diode current (I_D) comprises of the interesting and critical parameters of the three parameter model; shown in Equation 2.4, it

13
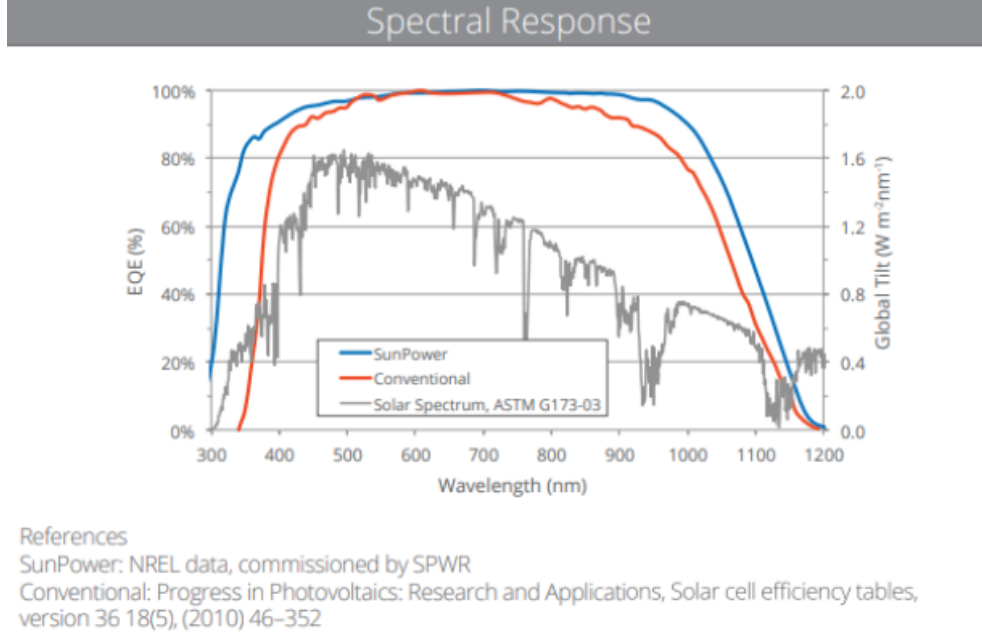
Figure 2.2: Maxeon Gen III Cell Spectral Response

consists of the term I_0 and an exponential. The exponential is a function of three key variables: the cell temperature (T_C), load voltage (V_L), and ideality factor (n).

$$I_D = I_0[\exp(\frac{V}{V_T}) - 1] \qquad \text{(A)} \quad (2.4)$$

This ideality factor is typically between 1 and 2, and represents the proportional influence of carriers inbseveral recombination processes for a given cell composition and structure. Some ideality factor values are presented in Table 2.1, sourced from PVEducation's Ideality Factor page [13]. We note that the ideality factor may be outside the typical range of $[1, 2]$, as discussed by Jain et Kapoor [14] and R.N. Hall [10], the latter of which notes that auger recombination dominated dark currents may generate a n of 2/3.

The term thermal voltage (V_T) (Equation 2.5) which encapsulates the cell temperature dependency describes the voltage across the P-N junction of the diode in the model: at STC this is typically 26 mV. We remind the reader that the remaining terms in this equation are the Boltzmann constant (K_B) and electric charge constant (q).

14

$$V_T = \frac{nk_BT_C}{q} \qquad \text{(V)} \quad (2.5)$$

Recombination Type	Ideality Factor	Description
SRH, band to band (low level injection)	1	Recombination limited by minority carrier.
SRH, band to band (high level injection)	2	Recombination limited by both carrier types.
Auger	2/3	Two majority and one minority carriers required for recombination.
Depletion region (junction)	2	Two carriers limit recombination.

Table 2.1: Various Ideality Factors of n

2.1.1.3 Dark Saturation Current

The dark saturation current, or reverse saturation current (I_0) has two potential derivations. Generally, the three parameter model, (see Baig et al. [2], MacAlpine et Brandemuehl [17], Rusirawan et Farkas [28], and others) define I_0 as in Equation 2.6; where the diode current is a function of the cell temperature and the energy bandgap in relation to several reference parameters at STC.

$$I_0 = I_{0,ref}\left(\frac{T_C}{T_{C,ref}}\right)^3 \exp\left(\frac{E_{G,ref}}{k_BT_{C,ref}} - \frac{E_G}{k_BT_C}\right) \qquad \text{(A)} \quad (2.6)$$

On the other hand, we can derive the I_0 algebraically: given the short short circuit current (I_{SC}) and open circuit voltage (V_{OC}), we can set the cell at open circuit, forming the derivation in Equation 2.7 and the result in Equation 2.8.

$$\begin{aligned} I_L &= 0 \\ &= I_{SC} - I_D \\ &= I_{SC} - I_0[\exp\left(\frac{V_{OC}}{V_T}\right) - 1] \end{aligned} \qquad \text{(A)} \quad (2.7)$$

$$I_0 = I_{SC}[\exp(\frac{V_{OC}}{V_T}) - 1]^{-1} \qquad\qquad \text{(A)} \quad (2.8)$$

The latter model is convenient since it does not require measuring reference dark saturation current at STC ($I_{0,ref}$), reference bandgap at STC ($E_{G,ref}$), nor bandgap (E_G). As such, we will focus on the latter model in subsection 2.1.4.

2.1.1.4 Short Circuit Current

Finally, for the three parameter model, we derive the dependence of short circuit current (I_{SC}) and open circuit voltage (V_{OC}) on irradiance (G) and cell temperature (T_C) before establishing the final derivation of Equation 2.1.

Starting with the short circuit current (I_{SC}), it is known that there is a large positive correlation with irradiance and a small positive correlation with temperature, shown in Figure 2.3 and Figure 2.4.

Figure 2.3: Solar Cell Temperature Dependence
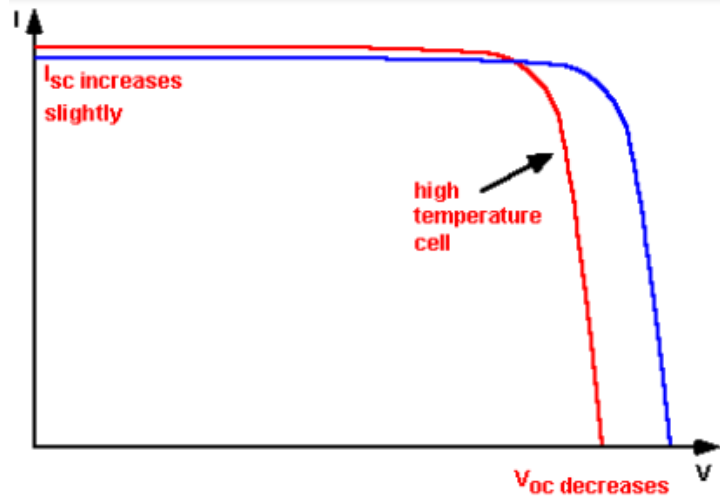
The dependence of irradiance on I_{SC} can be modeled as linearly proportional to the light incident upon the solar cell over the reference irradiance. This makes intuitive sense: given half the available light (assuming the distribution of light across the spectrum is consistent), the solar cell will only be able to capture half the maximum available power. Chegaar et al. [4]

16
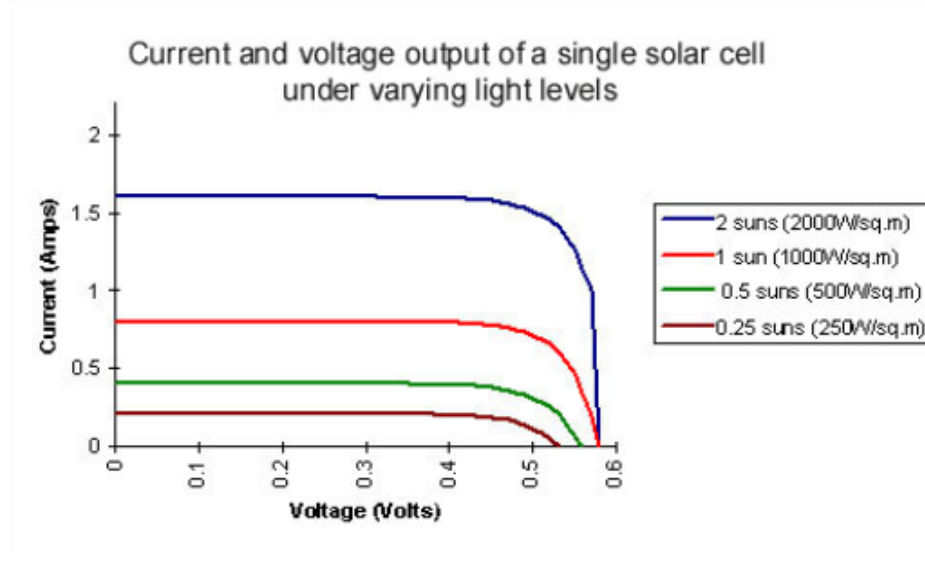
Figure 2.4: Solar Cell Irradiance Dependence

proposes this relationship as Equation 2.9, where the short circuit current is a function of short circuit current constant (K_E) and irradiance (G) (the latter in units of Wm^{-2}).

$$I_{SC}(G) = K_E G \qquad \text{(A)} \quad (2.9)$$

Equation 2.9 can be easily reworked where the constant K_E is now based on a reference short circuit current at STC ($I_{SC,ref}$) and a reference irradiance at STC (G_{ref}). This forms Equation 2.10, which is the same form used by Baig et al. [2].

$$I_{SC}(G) = I_{SC,ref} \frac{G}{G_{ref}} \qquad \text{(A)} \quad (2.10)$$

Hishikawa et al. [11] proposes modeling the dependence of temperature on I_{SC} using a short circuit current thermal coefficient (α) (Equation 2.11). α is empirically determined and varies given the material composition and structure of the solar cell; for crystalline silicon solar cells, this is approximately 0.05%/K, or 0.0005. Equation 2.11 can be rearranged to form Equation 2.12. This is effectively equivalent to Rusirawan et Farkas [28], but is slightly different from MacAlpine et Brandemuehl [17] and Baig et al. [2],

17

who take the constant term 1 and replace it with a another constant, $I_{SC,ref}$ (Equation 2.13).

$$\alpha = \frac{1}{I_{SC,ref}} \frac{\Delta I_{SC}}{\Delta T_C} = \frac{1}{I_{SC,ref}} \frac{I_{SC,ref} - I_{SC}}{T_{C,ref} - T_C} \qquad \text{(unitless)} \quad (2.11)$$

$$I_{SC}(T_C) = I_{SC,ref}[1 - \alpha(T_{C,ref} - T_C)] \qquad \text{(A)} \quad (2.12)$$

$$I_{SC}(T_C) = I_{SC,ref}[I_{SC,ref} - \alpha(T_{C,ref} - T_C)] \qquad \text{(A)} \quad (2.13)$$

These two competing models of the short circuit current will also be explored further in subsection 2.1.4. For now, we will combine Equation 2.10 and Equation 2.12 to give us Equation 2.14.

$$I_{SC}(G, T_C) = I_{SC,ref} \frac{G}{G_{ref}}[1 - \alpha(T_{C,ref} - T_C)] \qquad \text{(A)} \quad (2.14)$$

2.1.1.5 Open Circuit Voltage

Likewise, the open circuit voltage (V_{OC}) is also a function of temperature and irradiance. It is known that V_{OC} has a positive logarithmic correlation with irradiance and a medium negative correlation with temperature (Figure 2.3 and Figure 2.4).

Returning to Equation 2.8, in which we defined the dark saturation current, or reverse saturation current (I_0) as a function of V_{OC}, we can invert the equation to retrieve the V_{OC} parameter, shown in Equation 2.15.

$$V_{OC} = V_T \ln(\frac{I_{SC}}{I_0} + 1) \qquad \text{(V)} \quad (2.15)$$

There are three points in this equation that can now be determined. We know from Equation 2.5 that the thermal voltage (V_T) is dependent on the cell temperature (T_C). We can also plug in one of the proposed models for I_{SC}. However, we cannot reuse Equation 2.8 because Equation 2.15 was derived from it! Chegaar et al. [4] proposes an alternative form by simplifying the logarithmic term to form Equation 2.16.

$$V_{OC}(G, T_C) = V_{OC,ref} + V_T(T_C) \ln(\frac{G}{G_{ref}} + 1) \qquad \text{(V)} \quad (2.16)$$

18

This term fits well with the paper's experimental data, but has issues representing the voltage across the cell at low light conditions. Because the cell voltage is zero in complete darkness (there is no current generated because there is not potential difference between the terminals), we propose Equation 2.17, which is a modified form of Equation 2.16 that implements temperature dependence while retaining irradiance dependence.

$$V_{OC}(G, T_C) = V_{OC,ref}[1 - \beta(T_{C,ref} - T_C)]$$
$$+ \frac{nk_B(T_{C,ref} + T_C/\gamma)}{q} \ln(\frac{G}{G_{ref}}) \quad \text{(V)} \quad (2.17)$$

$$\beta = \frac{1}{V_{OC,ref}} \frac{\Delta V_{OC}}{\Delta T_C} = \frac{1}{V_{OC,ref}} \frac{V_{OC,ref} - V_{OC}}{T_{C,ref} - T_C} \quad \text{(unitless)} \quad (2.18)$$

Equation 2.17 implements two changes: a open circuit voltage thermal coefficient (β) and a thermal voltage modifier coefficient (γ). β is likewise (to α) empirically determined; for silicon it known to be -0.3%/K, or -0.003. γ is an experimentally determined curve fitting term, and affects how fast the logarithm converges to reference open circuit voltage at STC ($V_{OC,ref}$). It has an expected operable range of values between $[1, 100]$, where smaller values correlate to a wider range of of V_{OC} movement at low light conditions. This parameter, however, is not part of the three parameter cell model. Its efficacy will be explored further in subsection 2.1.4.

2.1.1.6 Model Summary

To conclude this section, we will review the components that make up the three parameter cell model, propose three items of further exploration, and propose a complete model function that incorporates the topics discussed.

Firstly, the three parameter cell model is composed of a constant current source and a power consuming diode, representing photogeneration and recombination effects of the solar cell, respectively. These two components form three parameters that is the namesake of this section, namely the photocurrent, dark saturation current, and ideality factor.

Secondly, we explore the construction and interpretation of these three components, and along the way, examine three areas that deviate from the existing models that we would like to investigate:

- an algebraic derivation of the dark saturation current, or reverse saturation current (I_0),

- an alternative interpretation of the short circuit current (I_{SC}) as a function of cell temperature (T_C),

- and a new thermal voltage modifier coefficient (γ) to improve open circuit voltage (V_{OC}) modeling at low lighting conditions.

Finally, we present the complete model and its derivation, in Equation 2.19. We observe that this complete model requires four reference parameters (note that in this paragraph we refer to parameters as in values that need to be determined and not larger terms used in the naming of the model):

- reference irradiance at STC (G_{ref})

- reference cell temperature at STC ($T_{C,ref}$)

- reference open circuit voltage at STC ($V_{OC,ref}$)

- reference short circuit current at STC ($I_{SC,ref}$)

and four curve fitting parameters:

- ideality factor (n)

- short circuit current thermal coefficient (α)

- open circuit voltage thermal coefficient (β)

- thermal voltage modifier coefficient (γ)

For the cells tested in this project, α and β were provided by the manufacturer, Maxeon, but n and γ were not. Curve fitting techniques such as simulated annealing are explored in subsection 2.1.4 to determine these two variables.

$$I_L(V_L, G, T_C) = I_{PV}(G, T_C) - I_D(V_L, G, T_C)$$
$$= I_{SC}(G, T_C) - I_D(V_L, G, T_C)$$
$$= I_{SC}(G, T_C) - I_0[\exp(\frac{V_L}{V_T(T_C)}) - 1]$$
$$= I_{SC}(G, T_C) - I_{SC}(G, T_C)[\exp(\frac{V_{OC}(G, T_C)}{V_T(T_C)}) - 1]^{-1}[\exp(\frac{V_L}{V_T(T_C)}) - 1]$$
$$= I_{SC}(G, T_C) - I_{SC}(G, T_C)\frac{\exp(\frac{V_L}{V_T(T_C)}) - 1}{\exp(\frac{V_{OC}(G, T_C)}{V_T(T_C)}) - 1}$$
$$= I_{SC}(G, T_C) - I_{SC}(G, T_C)\frac{\exp(\frac{qV_L}{nk_BT_C}) - 1}{\exp(\frac{qV_{OC}(G, T_C)}{nk_BT_C}) - 1}$$
$$= I_{SC}(G, T_C)[1 - \frac{\exp(\frac{qV_L}{nk_BT_C}) - 1}{\exp(\frac{qV_{OC}(G, T_C)}{nk_BT_C}) - 1}]$$
$$= I_{SC,ref}\frac{G}{G_{ref}}[1 - \alpha[T_{C,ref} - T_C]][1 - \frac{\exp(\frac{qV_L}{nk_BT_C}) - 1}{\exp(\frac{qV_{OC}(G, T_C)}{nk_BT_C}) - 1}]$$
$$= I_{SC,ref}\frac{G}{G_{ref}}[1 - \alpha[T_{C,ref} - T_C]]$$
$$* [1 + \frac{1 - \exp(\frac{qV_L}{nk_BT_C})}{1 - \exp(\frac{q[V_{OC,ref}[1-\beta[T_{C,ref}-T_C]] + \frac{nk_B(T_{C,ref}+T_C/\gamma)}{q}\ln(\frac{G}{G_{ref}})]}{nk_BT_C})}]$$

$$\text{(A)} \quad \text{(2.19)}$$

2.1.2   Five Parameter Solar Cell Model

The most common model for solar cells is the five parameter solar cell model, shown in Figure 2.5. This is the complete form of the single diode model discussed in the previous section, subsection 2.1.1. There are two added components/parameters: a series resistance (R_S) and shunt resistance (R_{SH}),
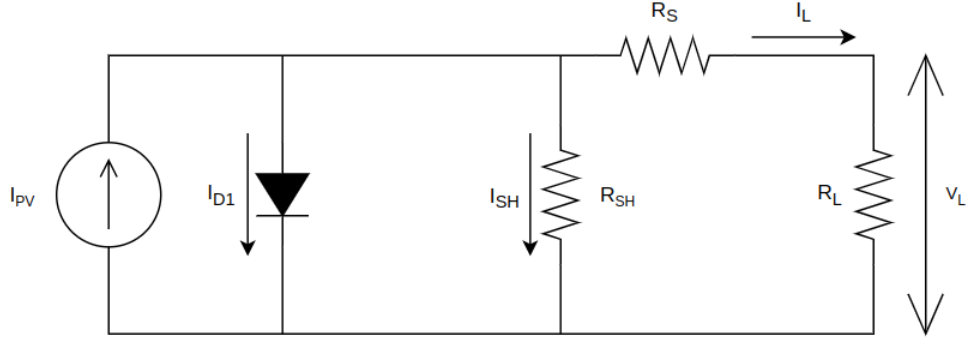
Figure 2.5: Five Parameter, or Full Single Diode Model of a Solar Cell

whose primary roles are to alter the shape of the knee-bend in the I-V curve. As such, this model improves upon the main flaw of the three parameter solar cell model, that of poorly predicting points clustering around the maximum power point.

In the following, we discuss the two added parameters and their specific effects on the model.

2.1.2.1   Shunt Resistance

Figure 2.6: Effect of Series (a) and Shunt Resistance (b) on I-V Curve

As shown in Figure 2.6 (b) from Nelson [23], as the shunt resistance (R_{SH}) decreases, the top of the knee-bend of the current-voltage (I-V) curve will be

22

forced down. At low values of R_{SH} (on the order of 10 Ω), the knee-bend will be pushed down so much that the curve becomes a straight line. At high values of R_{SH}, (on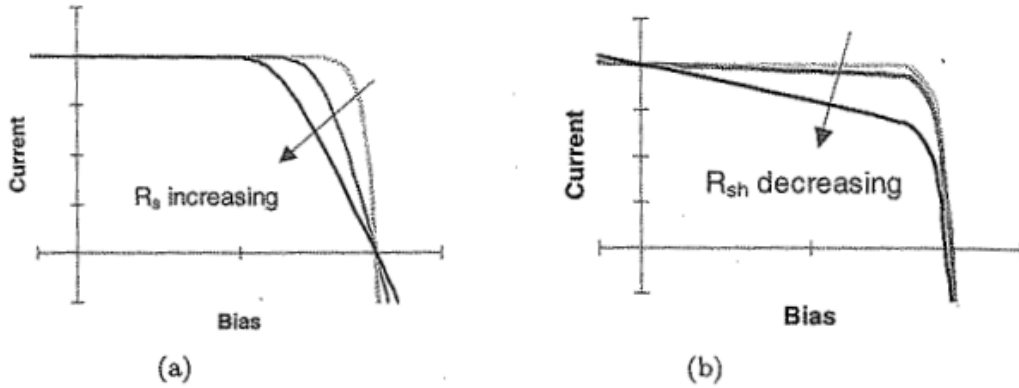 the order of 100 Ω), the curve converges to some fixed maximum bend constrained by other parameters of the model. This relationship is generally considered logarithmic.

The shunt current (I_{SH}) can be added to the simple form of the model as a new term as shown in Equation 2.20. Assuming that the series resistance (R_S) is negligible (0), we can determine that I_{SH} is a function of the R_{SH} and the load voltage (V_L), as shown in Equation 2.21.

$$I_L = I_{PV} - I_D - I_{SH} \qquad \text{(A)} \quad (2.20)$$

$$I_L = I_{PV} - I_D - \frac{V_L}{R_{SH}} \qquad \text{(A)} \quad (2.21)$$

2.1.2.2 Series Resistance

The series resistance (R_S) forces the knee-bend of the I-V curve to the left or right, as opposed to up and down for R_{SH}. As R_S increases, more current is consumed across the lumped resistance before reaching the terminals of the solar cell, reducing the expected current in the curve as shown in Figure 2.6 (a). At high values of R_S, the curve likewise becomes a straight line.

The R_S term impacts the consumers of the five parameter solar cell model; namely the I_D and the R_{SH} terms. A visualization of this is shown as Figure 2.7.

Revisiting Equation 2.4, we know that the dark current depends on load voltage (V_L) generated by load current (I_L) flowing through equivalent load resistance (R_L) connected at the cell terminals. This allows us to reformulate the dark current equation as Equation 2.22. Here, we add the voltage drop across the lumped series resistance summed with the V_L to represent the total voltage expected by the dark current model.

$$I_D = I_0[\exp(\frac{V_L + I_L R_S}{V_T}) - 1] \qquad \text{(A)} \quad (2.22)$$

We can likewise use the voltage drop to update the I_{SH} term, shown in Equation 2.23.

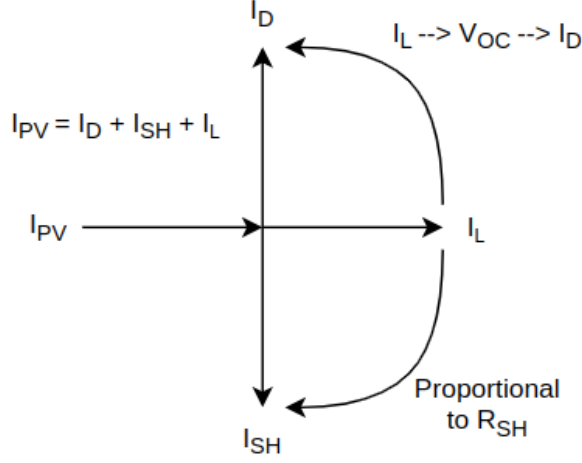$$I_{SH} = \frac{V_L + I_L R_S}{R_{SH}} \qquad \text{(A)} \quad (2.23)$$

23

Figure 2.7: Current Flow Junction of Five Parameter Model Solar Cell

Combining these two effects, we form Equation 2.24.

$$I_L = I_{PV} - I_0[\exp(\frac{V_L + I_L R_S}{V_T}) - 1] - \frac{V_L + I_L R_S}{R_{SH}} \qquad \text{(A)} \quad \text{(2.24)}$$

We note that this model is an implicit function and cannot easily (or prettily) move all the I_L terms to the left side of the equation. As such, for these types of problems, we will develop and use iterative solvers to determine I_L for a given set of input parameters (R_S, G, V_L, etc). Iterative solvers involve starting with a guess for the output parameter (in this case I_L) and attempt to improve upon that guess such that each side is equal to each other or within some tolerance to each other. An in depth discussion on how these solvers were implemented for this model and variants of this model can be found in **??**.

> Augment appendix note with reference to 2.1.4.5. Relegate appendix note to discussion about iterative solvers and steps to build iterative solver (Desmos - MATLAB - Python).

2.1.2.3 Photocurrent as a Function of Parasitics

An interesting addition to the five parameter cell model is presented by Cubas et al [5, 6]: they observe that Equation 2.24 in short circuit conditions results

in Equation 2.25.

$$I_{SC} = I_{PV} - I_0[\exp(\frac{I_{SC}R_S}{V_T}) - 1] - \frac{I_{SC}R_S}{R_{SH}} \qquad (A) \quad (2.25)$$

In their analysis of measurements taken across a broad spectrum of reference solar cells, represented in Table 2.2, the dark current at short circuit conditions were well less than a single milliampere, an insignificant fraction of the total operating current. From this observation Cubas et al. rewrites the above expression to get the photocurrent as a function of I_{SC} and a ratio of R_S and R_{SH}, shown in Equation 2.26.

$$I_{PV} = I_{SC}\frac{R_S + R_{SH}}{R_{SH}} \qquad (A) \quad (2.26)$$

Reference	Cell Type	I_{SC} (A)	$I_0[e^{\frac{I_{SC}R_S}{V_T}} - 1]$ (A)	I_D / I_{SC}
Kennerud, 1969	CdS	0.8040	1.56E-5	1.94E-5
Charles, 1981	BSC	0.1023	2.21E-8	2.16E-7
Charles, 1981	GSC	0.5610	1.01E-5	1.80E-5
Lo Brano, 2010	Q6LM	7.6650	1.42E-9	1.85E-10

Table 2.2: Dark Current Ratios for Various Reference Cells [5]

However, a cursory evaluation of the parameter space (V_{OC}, I_{SC}, G, T_C, R_S, n) reveals that the assumption that the dark current is negligible breaks down when a subset of the following conditions occur:

- the open circuit voltage (V_{OC}) becomes very small,

- the short circuit current (I_{SC}) becomes very large,

- and the series resistance (R_S) becomes relatively large for some combination of V_{OC} and I_{SC}.

Is it to be noted that these parameters are tightly coupled, and therefore the language specifying a parameter space upon which this term should be used remains imprecise. We also note that T_C and n when increased slightly tighten the viable parameter space.

However, when considering a specific solar cell that is *appropriate* (e.g. it contains STC defined parameters V_{OC} and I_{SC} with an measured R_S that results in negligible I_D), this term remains negligible unless the cell is exposed to (1) high temperatures or (2) high intensity light, two conditions that tend to come hand in hand. These conditions tend to only be experienced by concentrator photovoltaics and are highly unlikely to be reached by normal solar cells.

We will observe later in subsection 2.1.4 that with our dataset of Maxeon Gen III Bin Le1 solar cells, the vast majority of estimated series resistance is well below 0.08Ω, which results in dark currents less than a mA. This means that this modification (assuming it improves the accuracy of the model), is well suited for our solar cells.

Incorporating this revision, we arrive at Equation 2.27.

$$I_L = I_{SC}\frac{R_S + R_{SH}}{R_{SH}} - I_0[\exp(\frac{V_L + I_L R_S}{V_T}) - 1] - \frac{V_L + I_L R_S}{R_{SH}} \quad \text{(A)} \quad \text{(2.27)}$$

See https://www.desmos.com/calculator/nniw0mha2k to play around with the revised dark current model. Add as a figure later on compared to experimental data.

2.1.2.4 Parisitics as a Function of Irrad., Temp.

Throughout this discussion, we introduced the notion of shunt and series resistance as internal parasitics. However, we did not explore whether these 'internal parameters' are themselves affected by external conditions such as irradiance and temperature.

A comprehensive review and experimental paper from Fébba et al [7] performed experiments on solar cells to evaluate the effect of temperature and irradiance on shunt and series resistance, controlling for the two independent variables in ranges of 25°C to 55°C and 600W/m² to 1000W/m², respectively. Four figures, Figure 2.8 - Figure 2.11 are shown below to illustrate the following assertions.

For shunt resistance (R_{SH}), they observed the following trends:

- as temperature increases, the R_{SH} exponentially decays,

- and as irradiance increases, the R_{SH} linearly decreases.

For R_S, they observed the following trends:

- as temperature increases, the R_S exponentially decays,

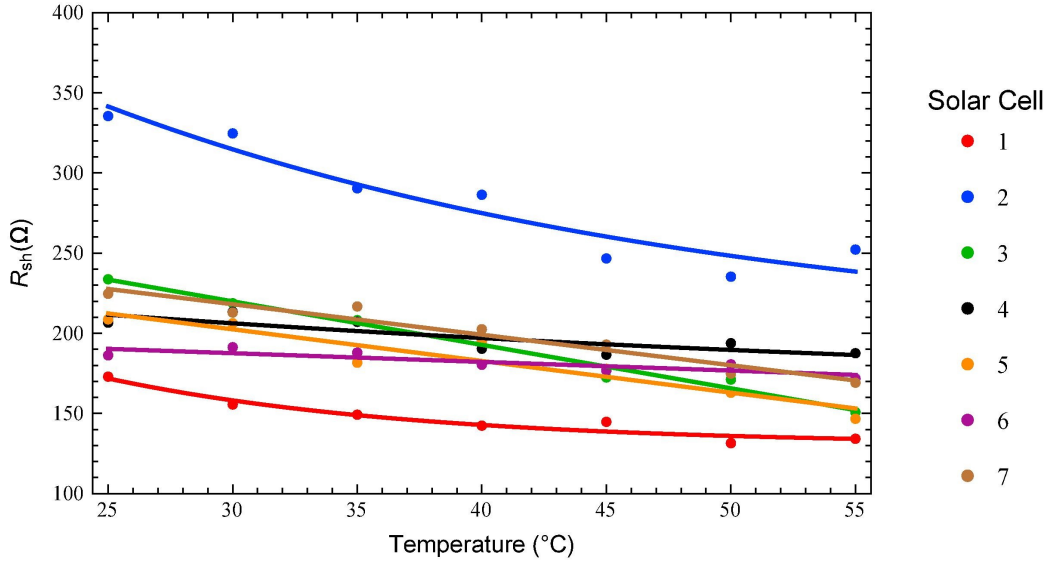- and as irradiance increases, the R_S linearly increases.

Figure 2.8: Shunt Resistance vs Temperature [7]

Fébba et al. did not posit a revised model of the either resistance term (although they did provide explanations on why the trends were reasonable), but Baig et al. [2] and MacAlpine et Brandemuehl [17] introduced a variant of Equation 2.28 that uses a series resistance thermal coefficient (ζ).

$$R_S = R_{S,ref} \exp(\zeta[T_{C,ref} - T_C]) \qquad (\Omega) \quad (2.28)$$

We extend Fébba et al [7]'s results to generate Equation 2.29, adding a series resistance irradiance coefficient (η), applied to Equation 2.28.

$$R_S = R_{S,ref} \exp(\zeta[T_{C,ref} - T_C])[1 + \eta(G_{ref} - G)] \qquad (\Omega) \quad (2.29)$$
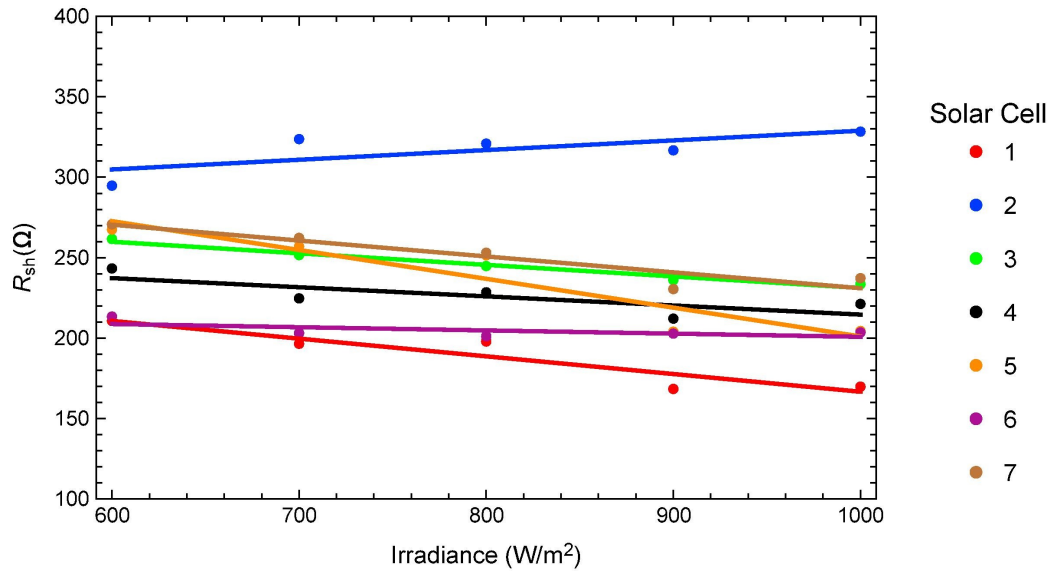
27

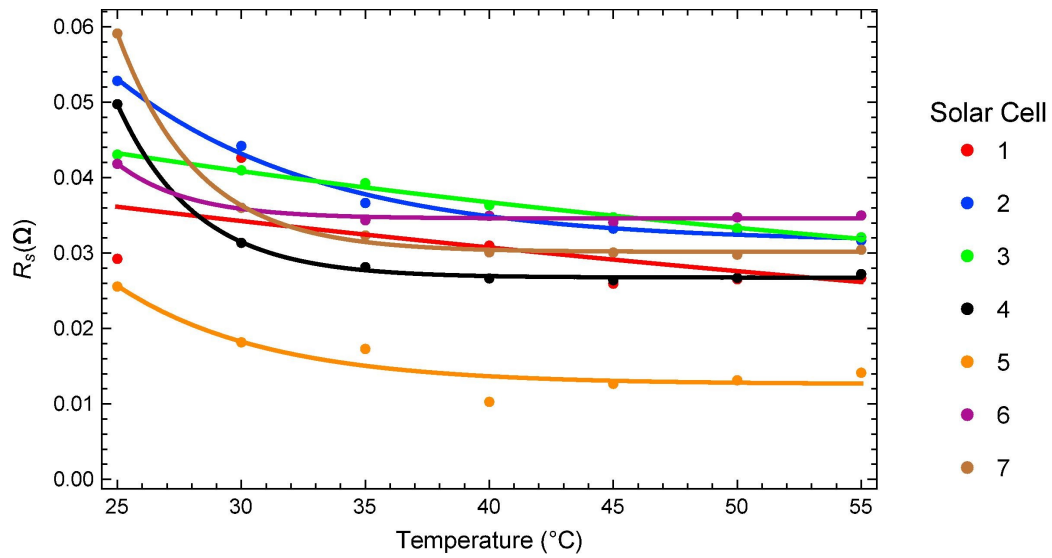Figure 2.9: Shunt Resistance vs Irradiance [7]

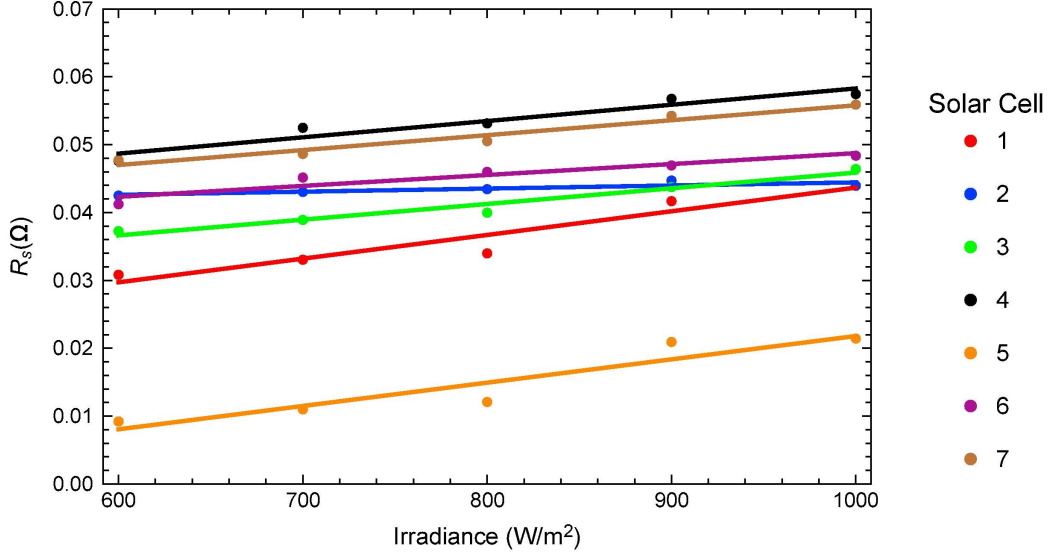Figure 2.10: Series Resistance vs Temperature [7]

Figure 2.11: Series Resistance vs Irradiance [7]

We also propose Equation 2.30 to model the shunt resistance, with shunt resistance thermal coefficient (κ) and shunt resistance irradiance coefficient (ι).

$$R_{SH} = R_{SH,ref} \exp(\kappa[T_{C,ref} - T_C])[1 + \iota[G_{ref} - G]] \qquad (\Omega) \quad (2.30)$$

Equation 2.29 and Equation 2.30's coefficients are not provided by the manufacturer, so they will have to be estimated. We'll look at ways to measure series and shunt resistance in **??**, and how to take advantage of our test setup to measure the coefficients. Additionally, we'll attempt to replicate Fébba et al's work on a broader scale, with a temperature and irradiance range of (0°C to 100°C and 0W/m² to 1000W/m², respectively).

2.1.2.5 Non Uniform Series Resistance

As an aside to this thesis, we note that the solar cell models described assume that the cell is uniform in composition and thus can represent the series resistance as a lumped resistance. In actuality, the cell is a two (actually three, but for all intents and purposes the thickness is irrelevant in terms of
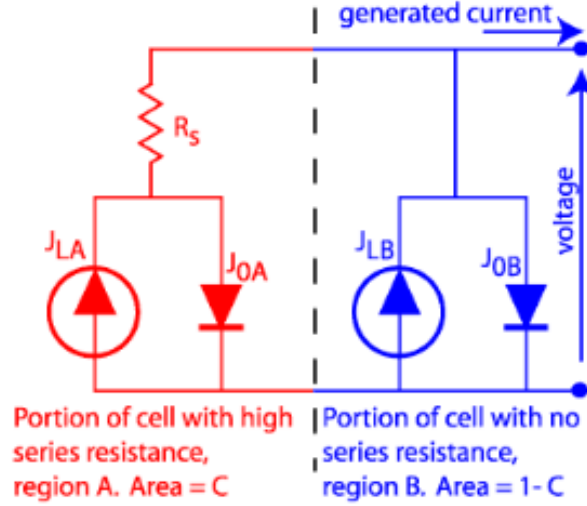
29

Figure 2.12: Solar Cell With Varying Series Resistances [20]

affecting the series resistance -although it may affect the shunt resistance) dimensional network of resistors and diodes (Figure 2.12).

If the cell series resistance was measured using two probes at various points in the cell, we would likely see that the places of smallest resistance will focus on the direct paths between two terminals; the places of largest resistance will be at the edges of the cell where the current path is longest. This is visualized on a Maxeon Gen III cell in Figure 2.13, where the darker paths represent higher resistances.

This series resistance non uniformity becomes more important to the resultant I-V curve in low light conditions. Under uniform, bright conditions, current from the photovoltaic effect is generated evenly and conducts to the contacts regardless of the resistance along the paths. In the dark, any current that has to flow through the cell (either from a partially unshaded region or from an external source) will favor the shortest/least resistive paths. As such, we would expect the apparent series resistance to vary in various lighting contexts.

For the purposes of this thesis, we will continue to assume that the solar cell, the base unit of our model, is uniform in internal and external characteristics. However, we will look at intercell variance in our module models. Further research into intracell series variance is explored by Bowden et Ro-
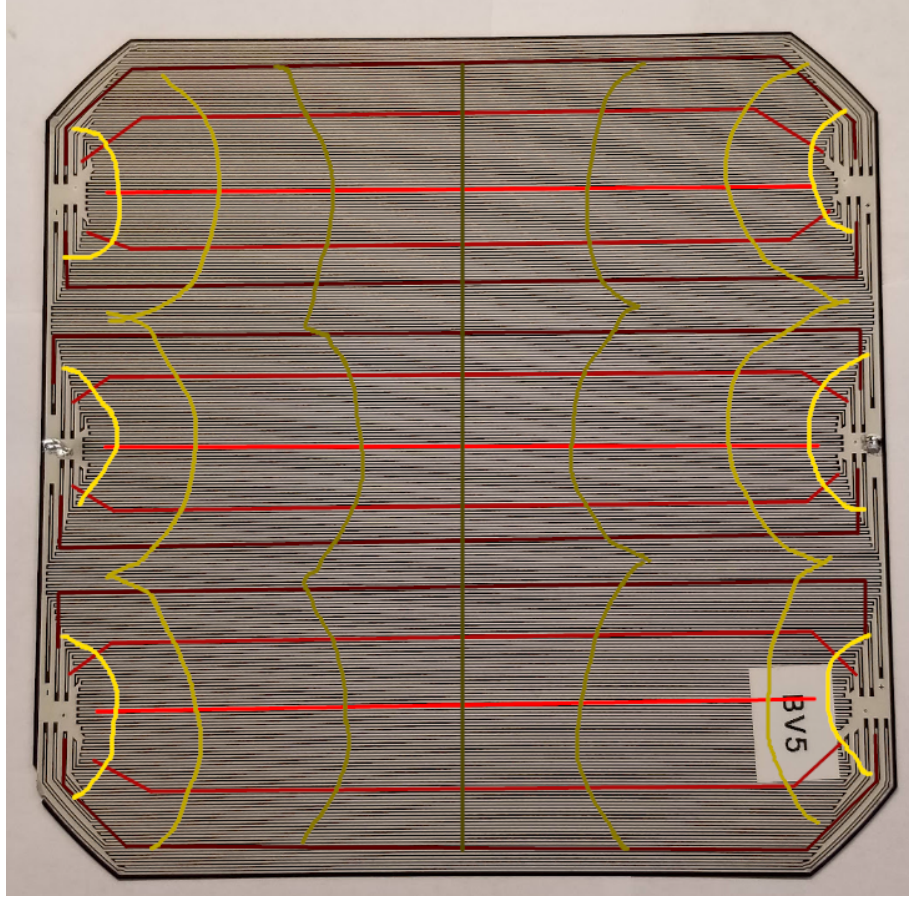
Figure 2.13: Current Paths of Maxeon Gen III Cell

hatgi [3].

2.1.2.6   Model Summary

To conclude this discussion, we will review the components that make up the five parameter cell model, propose an item of further exploration, and propose a complete model function that incorporates the topics discussed.

Firstly, the five parameter cell model retains the attributes of the three parameter cell model, being the complete form of the single diode model. It adds two parameters, a shunt resistance (R_{SH}) and series resistance (R_S) that represent ohmic losses in the solar cell, which primarily affect the knee-bend

of the resultant I-V curve. These two parameters help reduce error in the model around the knee-bend that cannot fully be represented by the ideality factor. However, these additions increase the complexity of the model, and the resultant form is an implicit equation that requires an iterative solver approach.

Secondly, we investigate a revision to the photocurrent model to make it also a function of R_S and R_{SH}. This was obtained by evaluating the short circuit condition of the existing model and reducing the dark current term under appropriate conditions. We note that this new model may not work under specific conditions, namely for concentrator solar cells or for solar cells with inordinately large series resistance relative to their specific V_{OC} and I_{SC} combination.

We also discuss evaluating R_S and R_{SH} themselves as a function of temperature and irradiance. We observe that these values tend to have exponential relationships with temperature and linear relationships with irradiance, although we require further data to validate the strength of these correlations. We derive initial models for these parameters, and discuss real world conditions in which they might deviate from our expectations (e.g. partial shading). As such, we will revisit both of these modifications to the base model in a further discussion to prove or disprove their veracity and usefulness to the overall model.

Finally, we incorporate these changes into the complete function defined in the previous sections. This is presented as Equation 2.31 (I_{SC}, V_{OC}, R_S, R_{SH}, and V_T abstracted out for clarity and brevity). We observe that this complete model builds upon the existing parameters named in subsubsection 2.1.1.6 by adding two extra reference parameters:

- reference series resistance at STC ($R_{S,ref}$)

- reference shunt resistance at STC ($R_{SH,ref}$)

and four more curve fitting parameters:

- series resistance thermal coefficient (ζ)

- series resistance irradiance coefficient (η)

- shunt resistance thermal coefficient (κ)

- shunt resistance irradiance coefficient (ι)

Likewise with the ideality factor (n) and thermal voltage modifier coefficient (γ) discussed in the three parameter solar cell model, we will look at estimating the four new curve fitting parameters using curve fitting and other statistical techniques. We can potentially establish known thermal coefficients (with some error) for these cells using the central limit theorem (CLT), and customize each cell with only the following variables: $R_{S,ref}$, $R_{SH,ref}$, which can be determined empirically using a single measurement at STC.

$$
\begin{aligned}
I_L(V_L, G, T_C) &= I_{PV}(G, T_C, R_S, R_{SH}) - I_D(V_L, G, T_C, R_S) - I_{SH}(R_S, R_{SH}) \\
&= I_{SC}(G, T_C)\frac{R_S + R_{SH}}{R_{SH}} - I_0(G, T_C)[\exp(\frac{V_L + I_L R_S}{V_T(T_C)}) - 1] - \frac{V_L + I_L R_S}{R_{SH}} \\
&= I_{SC}(G, T_C)\frac{R_S + R_{SH}}{R_{SH}} - I_{SC}(G, T_C)\frac{\exp(\frac{V_L + I_L R_S}{V_T(T_C)}) - 1}{\exp(\frac{V_{OC}(G, T_C)}{V_T(T_C)}) - 1} - \frac{V_L + I_L R_S}{R_{SH}} \\
&= I_{SC}(G, T_C)[\frac{R_S + R_{SH}}{R_{SH}} + \frac{1 - \exp(\frac{V_L + I_L R_S}{V_T(T_C)})}{1 - \exp(\frac{V_{OC}(G, T_C)}{V_T(T_C)})}] - \frac{V_L + I_L R_S}{R_{SH}}
\end{aligned}
$$

$$\text{(A)} \quad \text{(2.31)}$$

See https://www.desmos.com/calculator/yp0rhmabkz to play around with the complete five parameter solar cell model. Add as a figure later on compared to experimental data.

2.1.3 Seven Parameter Solar Cell Model

The seven parameter solar cell model (Figure 2.14), also known as a double diode model, builds upon the five parameter model by introducing a second diode (hence the name) to more accurately model internal current losses.

These losses can be split into the following:

- losses due to carrier recombination in the space charge region of the P-N junction,

- and losses due to surface recombination.

These currents are denoted as carrier recombination dark current (I_{D1}) and surface recombination dark current (I_{D2}), respectively. By differentiating
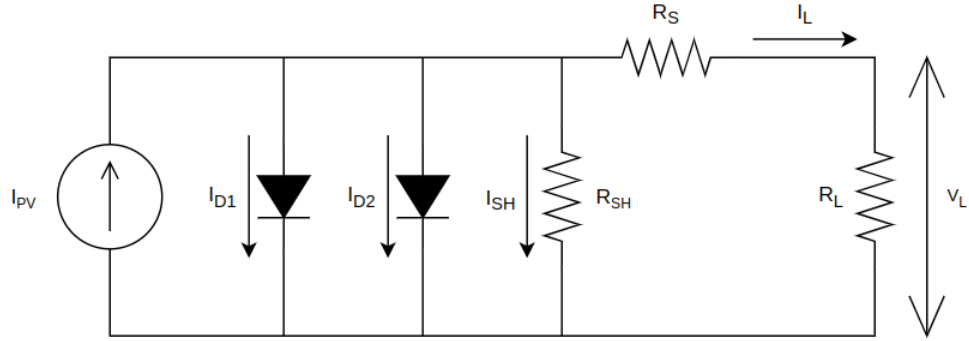
Figure 2.14: Seven Parameter, or Double Diode Model of a Solar Cell

between the two primary recombination processes in the cell, the seven parameter model is generally considered more accurate than the five parameter model.

The general form of this equation is shown in Equation 2.32.

$$I_L = I_{PV} - I_{D1} - I_{D2} - I_{SH} \qquad \text{(A)} \quad (2.32)$$

This results in the Equation 2.33 when all components have been inserted:

$$\begin{aligned}
I_L(V_L, G, T_C) &= I_{PV}(G, T_C, R_S, R_{SH}) - I_{D1}(V_L, G, T_C, R_S) - I_{D2}(V_L, G, T_C, R_S) \\
&\quad - I_{SH}(R_S, R_{SH}) \\
&= I_{SC}(G, T_C)\frac{R_S + R_{SH}}{R_{SH}} - I_{01}(G, T_C)[\exp(\frac{q[V_L + I_L R_S]}{n_1 k_B T_C}) - 1] \\
&\quad - I_{02}(G, T_C)[\exp(\frac{q[V_L + I_L R_S]}{n_2 k_B T_C}) - 1] - \frac{V_L + I_L R_S}{R_{SH}} \\
&= I_{SC}(G, T_C)\frac{R_S + R_{SH}}{R_{SH}} - I_{SC}(G, T_C)\frac{\exp(\frac{q[V_L + I_L R_S]}{n_1 k_B T_C}) - 1}{\exp(\frac{q V_{OC}(G, T_C)}{n_1 k_B T_C}) - 1} \\
&\quad - I_{SC}(G, T_C)\frac{\exp(\frac{q[V_L + I_L R_S]}{n_2 k_B T_C}) - 1}{\exp(\frac{q V_{OC}(G, T_C)}{n_2 k_B T_C}) - 1} - \frac{V_L + I_L R_S}{R_{SH}} \\
&= I_{SC}(G, T_C)[\frac{R_S + R_{SH}}{R_{SH}} + \frac{1 - \exp(\frac{q[V_L + I_L R_S]}{n_1 k_B T_C})}{1 - \exp(\frac{q V_{OC}(G, T_C)}{n_1 k_B T_C})} \\
&\quad + \frac{1 - \exp(\frac{q[V_L + I_L R_S]}{n_2 k_B T_C})}{1 - \exp(\frac{q V_{OC}(G, T_C)}{n_2 k_B T_C})}] - \frac{V_L + I_L R_S}{R_{SH}}
\end{aligned}$$

$$\text{(A)} \quad \text{(2.33)}$$

We note in this equation V_T was substituted back in to demonstrate that each ideality constant for each diode is unique.

$$I_L(V_L, G, T_C) = I_{SC,ref} \frac{G}{G_{ref}} [1 - \alpha(T_{C,ref} - T_C)]$$

$$\Big[$$

$$\frac{R_{S,ref} \exp(\zeta[T_{C,ref} - T_C])[1 + \eta(G - G_{ref})]}{R_{SH,ref} \exp(\kappa[T_{C,ref} - T_C])[1 - \iota(G - G_{ref})]} + 1$$

$$+ \frac{1 - \exp\left(\frac{q[V_L + I_L R_{S,ref} \exp(\zeta[T_{C,ref} - T_C])[1 + \eta(G - G_{ref})]]}{n_1 k_B T_C}\right)}{1 - \exp\left(\frac{q[V_{OC,ref}[1 - \beta(T_{C,ref} - T_C)] + \frac{n k_B (T_{C,ref} + T_C/\gamma)}{q} \ln(\frac{G}{G_{ref}})](G, T_C)}{n_1 k_B T_C}\right)}$$

$$+ \frac{1 - \exp\left(\frac{q[V_L + I_L R_{S,ref} \exp(\zeta[T_{C,ref} - T_C])[1 + \eta(G - G_{ref})]]}{n_2 k_B T_C}\right)}{1 - \exp\left(\frac{q[V_{OC,ref}[1 - \beta(T_{C,ref} - T_C)] + \frac{n k_B (T_{C,ref} + T_C/\gamma)}{q} \ln(\frac{G}{G_{ref}})](G, T_C)}{n_2 k_B T_C}\right)}$$

$$\Big]$$

$$- \frac{V_L + I_L R_{S,ref} \exp(\zeta[T_{C,ref} - T_C])[1 + \eta(G - G_{ref})]}{R_{SH,ref} \exp(\kappa[T_{C,ref} - T_C])[1 - \iota(G - G_{ref})]}$$

$$(A) \quad (2.34)$$

2.1.3.1 Model Summary

2.1.4 Evaluation of Solar Cell Models

To evaluate these solar cell models and their proposed modifications, we used a set of almost 450 Maxeon Gen III and Maxeon C60 solar cells. In the following, we discuss how we characterized these solar cells using custom

36

hardware (HW) and software (SW) to generate a robust dataset. We'll look at the dataset distributions and compare them against the manufacturer specifications, and finally, we'll use these extracted parameters to compare the models with the data to determine model accuracy and precision.
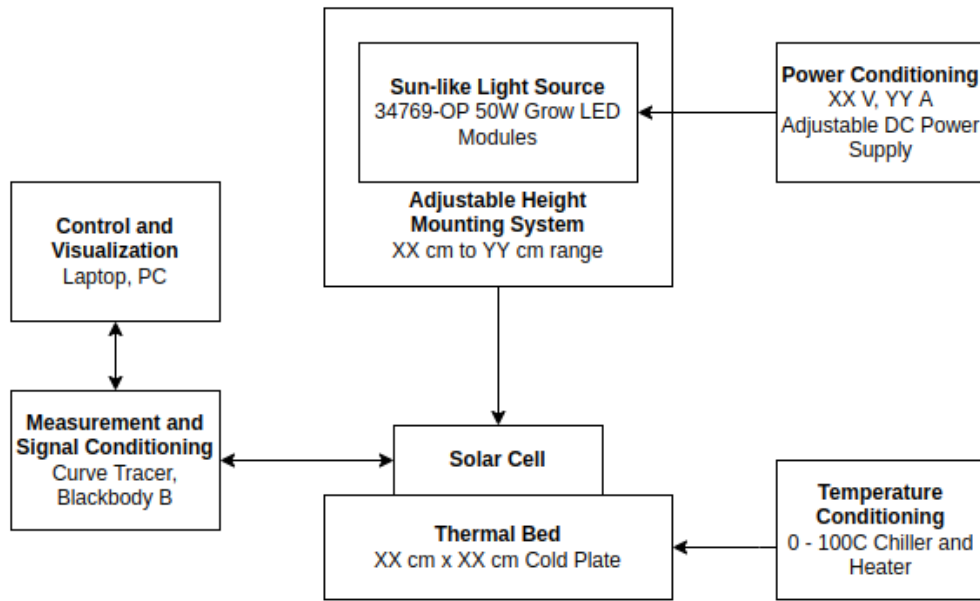
2.1.4.1 Solar Cell Test Setup

Figure 2.15: Photovoltaic Testing Setup

To characterize solar cells, we developed a test setup as outlined in Figure 2.15. In this test setup, we maintain three critical requirements:

- The test article experiences irradiance and temperature that is *temporally* and *spatially* uniform.

- The test article experiences a *measurable* irradiance and temperature.

- The irradiance and temperature experienced by the test article can be physically manipulated.

To achieve these aforementioned requirements, we first use a solar simulator consisting of a set of grow light modules (MPJA 34769-OPs) mounted to an aluminum plate heatsink. The MPJA grow light modules have an emittance spectra as shown in Figure 2.17; compared to the AM1.5 solar spectra (in particular, ASTMG173) in Figure 2.16, it can be said that these LEDs are not a great characterization of natural sunlight. A proposed design of a multi-channel LED based solar simulator is presented in Appendix C, following after similar efforts by others [16, 25, 1, 22], but that is beyond the scope of this thesis.
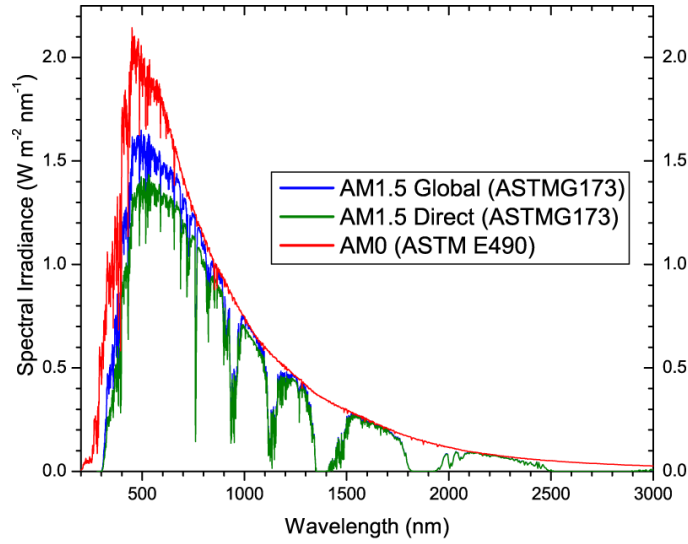

Figure 2.16: AM0, AM1.5 Solar Spectra

Add reference to AMS TSL2591 datasheet. Figure 11.

To ensure that the solar simulator irradiance is temporally uniform, a low cost luminosity sensor (TSL2591) is used to measure the irradiance over a fixed period of time. This period of time should be long enough to determine whether the lights have a warm up time and change in irradiance over the expected experiment duration. In order to get irradiance, we must convert the TSL2591 'counts' into watt/m^2; this is not straightforward, since the normalized responsivity spectrum of the TSL2591 (Figure 2.18) is also quite divergent from AM1.5G solar spectrum. It is, however, relatively close to the absorbance spectra observed by the Maxeon Gen III solar cells, so the irradiance measured by the device will closely match (if not slightly undershoot)
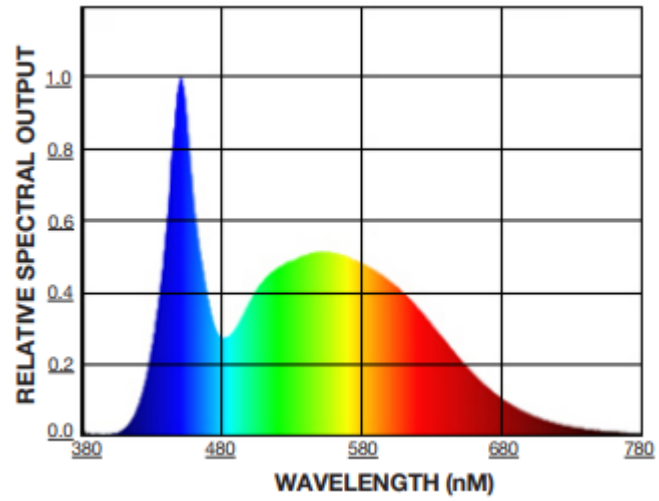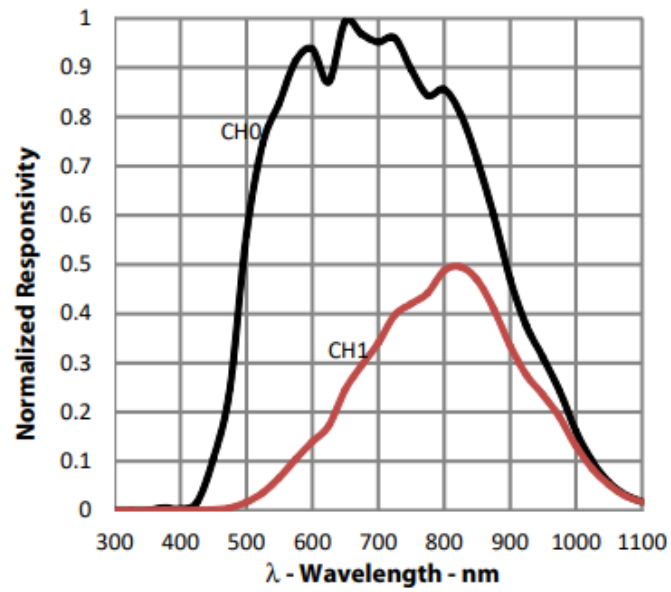
Figure 2.17: MPJA Grow Light Spectrum

Figure 2.18: TSL2591 Spectral Responsivity

the expected value captured by the cell. A further discussion on methods to calibrate the sensor readings for a true observed solar spectra is presented in Appendix D. These calibration methods are useful for testing photovoltaics outdoors.

To ensure the solar simulator irradiance is spatially uniform, the lighting modules relative to each other and relative to the plate need to be spaced appropriately. The light modules have a nonuniform intensity profile (e.g. light is concentrated radially from the center of the fixture), and thus require some overlap in illuminance area to create a superimposed, roughly uniform light distribution. The spacing is empirically evaluated by also using the TSL2591, similar to how photosynthetic photon flux density (PPFD) is measured [9]: a closely spaced set of points is mapped to their respective intensity measurements to determine the variance in intensity and the lights are moved closer/farther apart accordingly to minimize said variance.

The photovoltaic, a solar cell or solar module of up to 500mm by 250mm (equivalent to 4 cells by 2 cells) in size, is placed upon a thermal bed separated by a thin, electrically insulating layer of Kapton tape; this thermal bed maintains the photovoltaic surface temperature via conductance, and pumped distilled water is circulated through the bed by a XXX.

Insert name of heater/ chiller device

After controlling for the light intensity and temperature of the test article, the actual measurement of the solar cell parameters is performed by custom PCBs developed by the team. The primary PCB measures the I-V curve of the photovoltaic by adjusting the perceived load across the terminals. It does this by actuating a pair of high power metal-oxide-semiconductor field-effect transistors (MOSFETs), particularly in the ohmic region between open and short circuit. Small steps to the gate voltage combined with a current and voltage sensor allow for high resolution measurements of the test article. These measurements are communicated back to the user via universal serial bus (USB) and captured using the Python scripting language. This allows us to communicate to the device to set measurement profiles using either a command line interface (CLI) or GUI. A secondary PCB containing the TSL2591 is also hooked up to the primary PCB via a controller area network (CAN) hardware interface. This allows us to also combine irradiance measurements with the electrical measurements and appropriately obtain predicted parameters at STC. A further description of the hardware and software implementation of these two PCBs are provided in Appendix E and Appendix F.

These elements of the test setup are depicted in Figure 2.19.
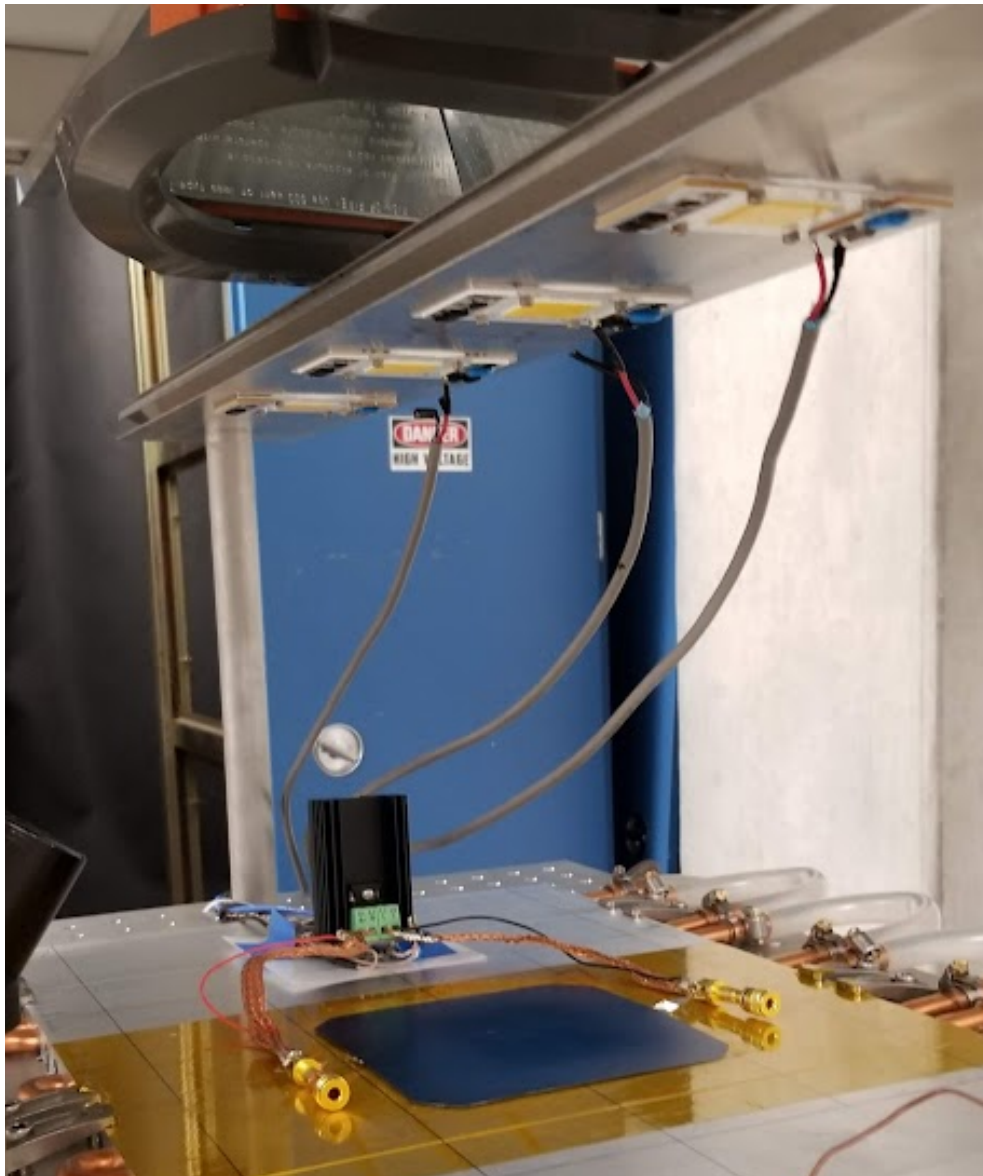
Figure 2.19: Photovoltaic Testing Setup

2.1.4.2 Solar Cell Characterization

The actual process of characterizing solar cells is now described as follows.

1. The test article is labeled with a unique identifier (e.g. BV101) (Figure 2.20). This identifier is placed on the positive terminal of the cell, preferably in a consistent orientation, to facilitate quick identification and manipulation of the cell.

Figure 2.20: Solar Cell Label Placement

2. Leads are soldered on to the edge contacts of the test article, taking care to make sure that there are no solder bumps left after soldering nor excess solder bridging traces, causing a short (Figure 2.21).
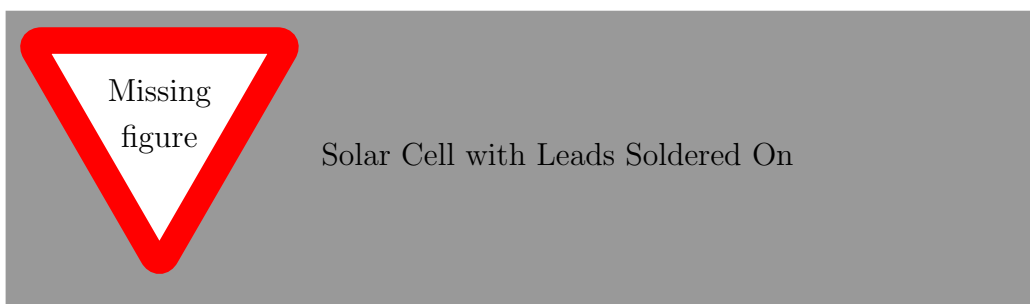

Figure 2.21: Solar Cell with Leads Soldered On

3. The test article is placed on top of the kapton tape layer in the test setup, centering the article to the guide lines marked that correspond to the positions of the abovehead grow lights (Figure 2.22).
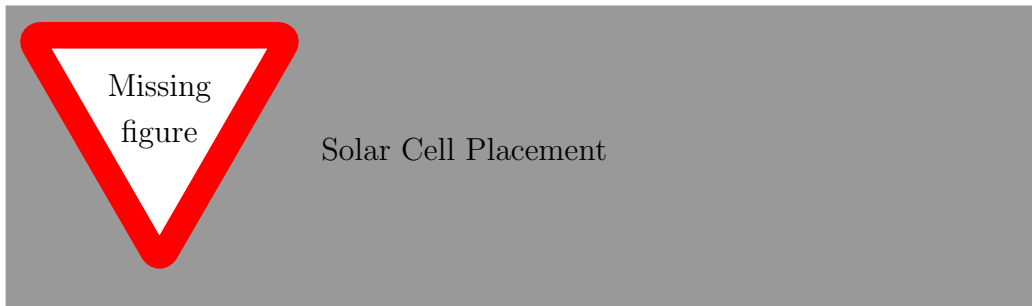
Figure 2.22: Solar Cell Placement

4. The primary PCB connects four wires to the cell leads; two thick wires for current measurement and two thin wires for voltage measurement (Figure 2.23).

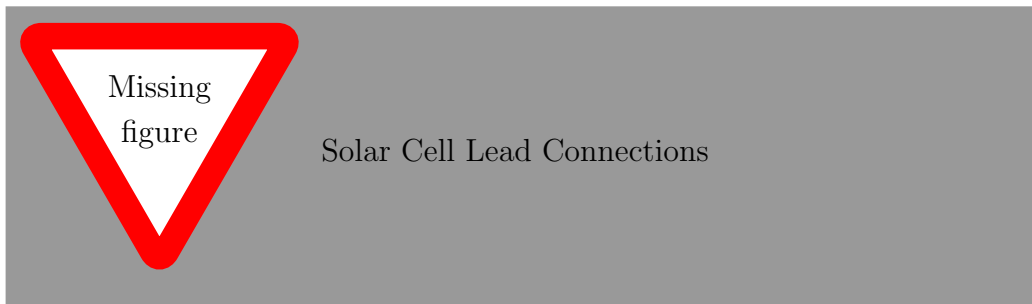Figure 2.23: Solar Cell Lead Connections

5. The primary PCB is connected via USB to a computer with our custom application installed (Figure 2.24).

6. We specify the conditions of the test (e.g. PV identifier, type of PV, step size, sample averaging control, test duration, etc) and initialize the PCB (Figure 2.25).

7. We enable the lighting and thermal conditioning equipment, modifying irradiance and temperature as expected (Figure 2.26).

8. We start the PCB, which begins a scan of the PV for the specified duration. The application then proceeds to capture the data from the
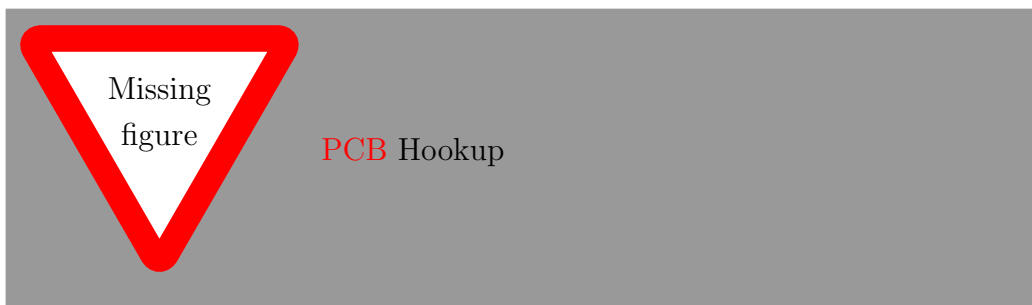
Figure 2.24: PCB Hookup
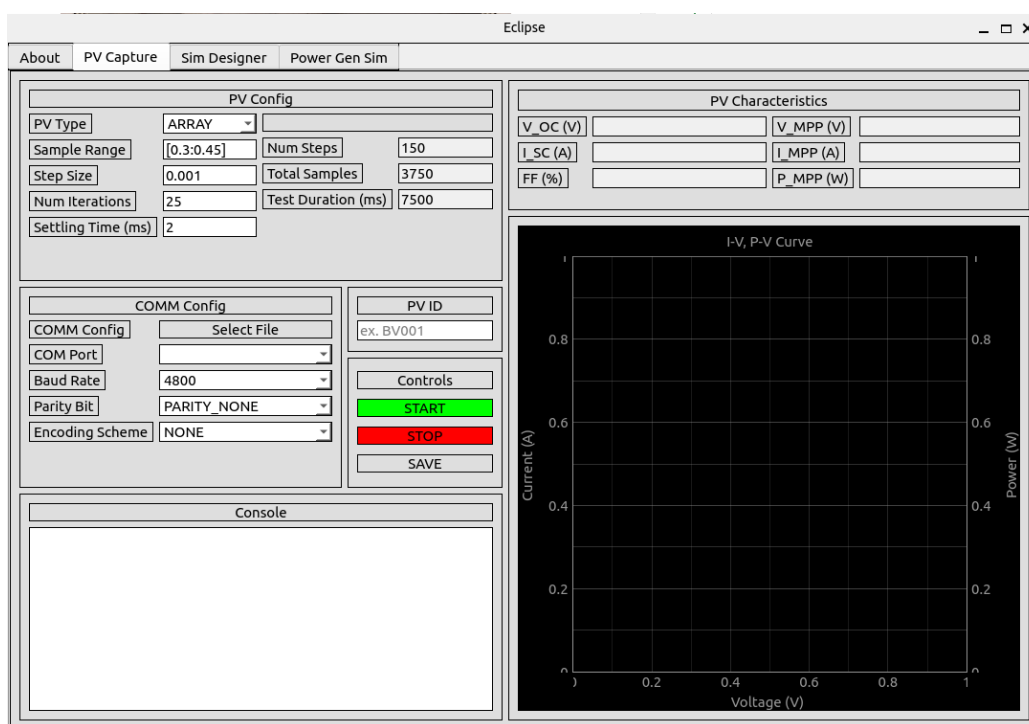

Figure 2.25: User Application GUI

Figure 2.26: Equipment Setup

PCB and visualize it as well as extract important parameters from cell (Figure 2.27).

Figure 2.27: Cell Results

9. Finally, the lighting and thermal conditioning equipment are turned off, the cell is disconnected from the setup, and the leads are desoldered.

An optional action is that we can hook up the secondary PCB that measures the irradiance from the test setup prior to placing the solar cell (Figure 2.28). This allows the primary PCB to also return the expected cell irradiance to the user application, which will automatically adjust and predict the curve at STC (Figure 2.29).

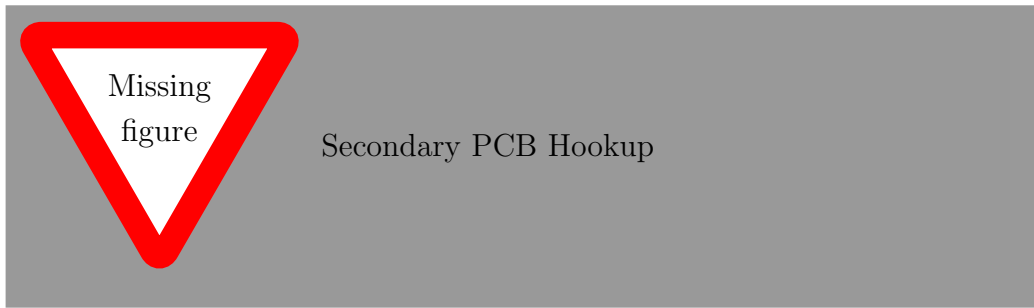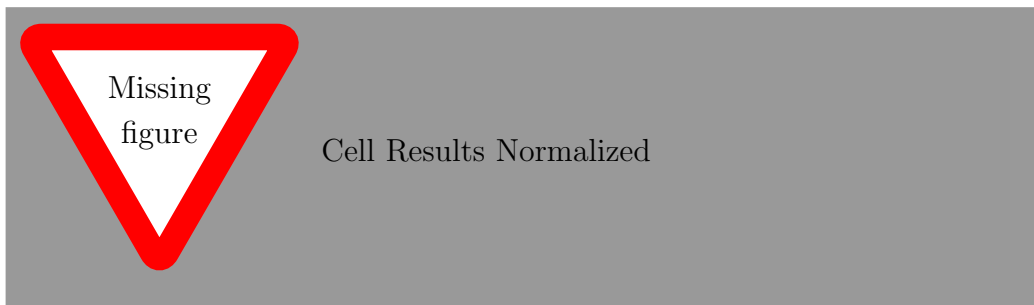Figure 2.28: Secondary PCB Hookup

Figure 2.29: Cell Results Normalized

2.1.4.3 Extraction of Cell Parameters

1. Scatter plot of I-V, P-V curves

2. Review of parameters that need to be measured:

   - irradiance (G)
   - cell temperature (T_C)
   - open circuit voltage (V_{OC})
   - short circuit current (I_{SC})
   - series resistance (R_S)
   - shunt resistance (R_{SH})
   - short circuit current thermal coefficient (α)
   - open circuit voltage thermal coefficient (β)
   - series resistance thermal coefficient (ζ)
   - series resistance irradiance coefficient (η)
   - shunt resistance thermal coefficient (κ)
   - shunt resistance irradiance coefficient (ι)
   - ideality factor of space charge recombination (n_1)
   - ideality factor of surface recombination (n_2)
   - thermal voltage modifier coefficient (γ)

3. Empirical Measurement of G to R_{SH}

4. Empirical Measurement of α to ι

5. Statistical Measurement of n_1 to γ

6. Evaluation of parameter distributions

7. Comparison of distribution against smith et al [29]

2.1.4.4 Solar Cell Dataset

The solar cells used for the LHRs solar vehicle are a mixture of Maxeon Gen III and Maxeon C60 solar cells. These solar cells were selected primarily due to financial and availability constraints; historically, in the last two solar vehicle revisions (2018, 2021) Gen III Bin Le1 cells have been used, but this year the team decided to procure cheaper, more easily available C60 cells from secondary suppliers. Regardless, these cell lines remain state of the art despite their age[1]; both Aptera Motors [30] and Lightyear One [8] -the latter of which is a former competitive solar vehicle team- have announced cooperation with Maxeon to use their solar cells. Aptera in particular uses the Gen III cells [30].

While these cell types are both 125mm by 125mm (see Figure 2.30 for a visualization of the cell physical layout), the Gen III cells are slightly more efficient than the C60 cells. Their (Gen III) rear contacts also tend to be slightly narrower than the C60 cells. Their electrical characteristics are outlined in Figure 2.31 and Figure 2.32. Note that the Maxeon Gen III cells are explicitly Bin Le1 cells, although the dataset will later show that the binning for both groups of cells tends to not be very respective of the actual measured I-V curves, which is likely due to the variance in our testing setup.

Since these cells were unpacked and designated for specific years, Table 2.3 is provided to delineate between the different types and 'lines' of cells tested. 'Lines' in this sense indicate the academic year the cells were originally unpacked and tested.

Cell Line	Year Unpacked	Type	Number of Cells
RP	2022	C60	X
MW	2020	Gen III	X
2019_Le1	2019	Gen III	X
BU	2018	Gen III	X

Table 2.3: Cell Lines Used in Solar Cell Dataset

Add number of cells tested to each group in table.

---

[1]the dates are unclear, but it appears that C60 was introduced around 2007 [12] and the Gen III has been around as long as 2013 [29].

Cell Physical Characteristics

Wafer:	Monocrystalline silicon
Design:	All back contact
Front:	Uniform, black antireflection coating
Back:	Tin-coated, copper metal grid
Cell Area:	Approximately 153cm²
Cell Weight:	Approximately 6.5grams
Cell Thickness:	150μm +/- 30μm

Bond pad detail with positive indicator

5.4

+

125

3.0

3.0

160

125

Positive Bond Pads

Dimensions in mm

38.5   38.5

Bond pad area dimensions are 5.4mm x 3.0mm
Metal finger pitch between positive and negative fingers is 471um.
Positive/Negative pole bond pad sides have "+/-" indicators on leftmost and rightmost bond pads
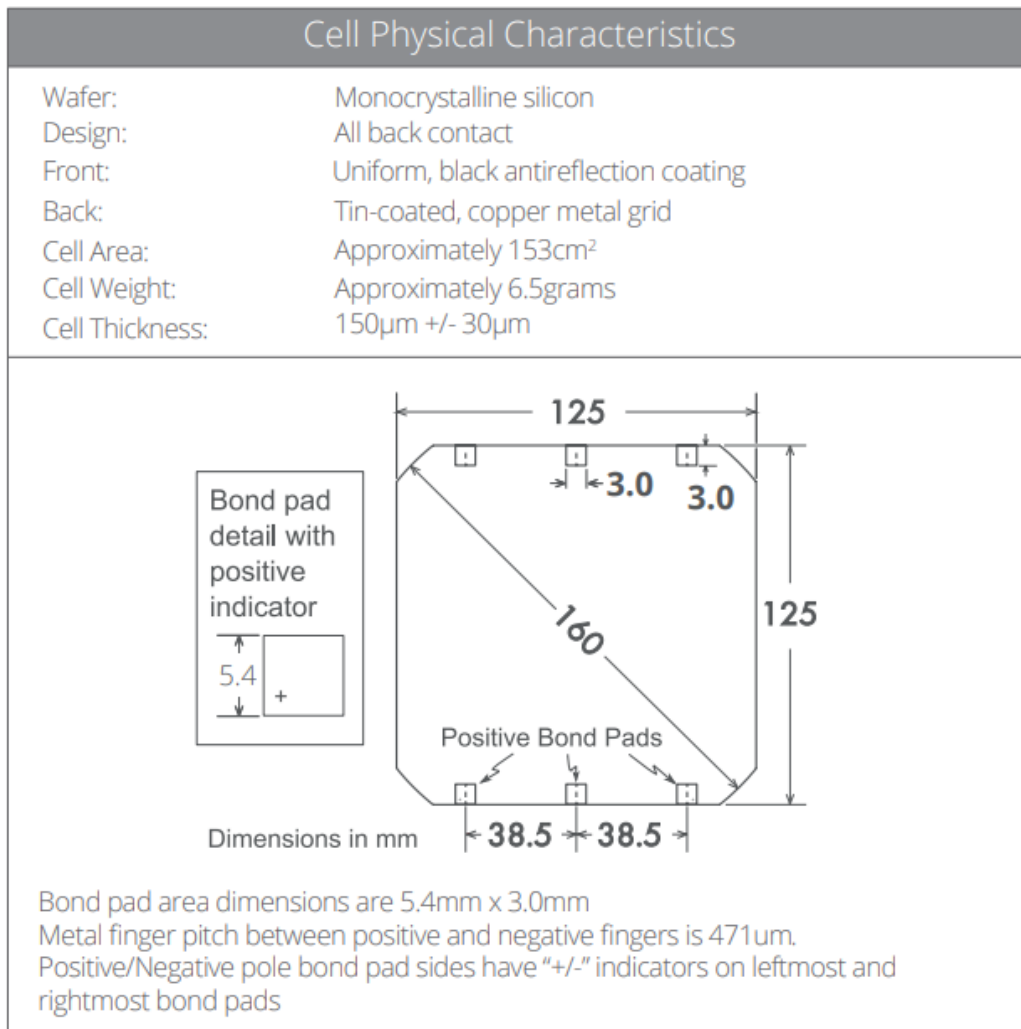
Figure 2.30: Maxeon Gen III Cell Footprint

Electrical Characteristics of a typical Maxeon Gen III Cell At Standard Test Conditions (STC) STC: 1000W/m² , AM 1.5G and cell temp 25°C							
	Cell Bin	Pmpp (Wp)	Eff. (%)	Vmpp (V)	Impp (A)	Voc (V)	Isc (A)
Ultra Peak Performance	Me1	3.72	24.3	0.632	5.89	0.730	6.18
Ultra Premium Performance	Le1	3.63	23.7	0.621	5.84	0.721	6.15
Ultra High Performance	Ke1	3.54	23.1	0.612	5.79	0.713	6.11

Electrical parameters are nominal values.
Temp.Coefficients in SunPower Panels: Voltage: -1.74mV/°C, Current: 2.9mA/°C, Power: -0.29%/°C

Figure 2.31: Maxeon Gen III Cell Characteristics

Electrical Characteristics of Typical Cell at Standard Test Conditions (STC) STC: 1000W/m² , AM 1.5g and cell temp 25°C						
Bin	Pmpp (Wp)	Eff. (%)	Vmpp (V)	Impp (A)	Voc (V)	Isc (A)
G	3.34	21.8	0.574	5.83	0.682	6.24
H	3.38	22.1	0.577	5.87	0.684	6.26
I	3.40	22.3	0.581	5.90	0.686	6.27
J	3.42	22.5	0.582	5.93	0.687	6.28

All Electrical Characteristics parameters are nominal
Unlaminated Cell Temperature Coefficients
Voltage: -1.8 mV / °C   Power: -0.32% / °C

Figure 2.32: Maxeon C60 Cell Characteristics

1. Evaluation of parameter distributions

2. Comparison of distributions against smith et al [29]

2.1.4.5 Modeling Solar Cell Datasets

1. Evaluate initial Desmos models using datasheet parameters

2. Compare secondary Python models using extracted parameters against cell I-V curves.

2.1.4.6 Results

Holistic evaluation w/ table on statistics of model: e.g. for a given model and extracted cell parameters, what is the overall cell line accuracy and precision?

2.2 Modeling Solar Modules

After modeling the solar cell, the next layer up in the abstraction chain is modeling a solar module. A solar module, in a typical configuration, may consist of several solar cells in series, also called a 'string'. For the LHRs vehicle, we place many modules in series with each other before terminating at our variable load, a maximum power point tracking (MPPT). In our configuration, for each module, we place a 'bypass diode' in antiparallel to each module. This is used to provide an alternative path of current to flow in the event that a solar module is insufficient for driving the current. This could happen if a single (or several) solar cell(s) in the module is (are) broken, or shaded, or some combination of the two.

In this section, we'll focus on the conditions that cause issues with solar modules, in particular, cell mismatch. We'll look at how cells with differing operating conditions in series can drag down the efficiency of the module, and we'll incorporate the bypass diode into the model and investigate the conditions in which it activates and to what degree it activates.

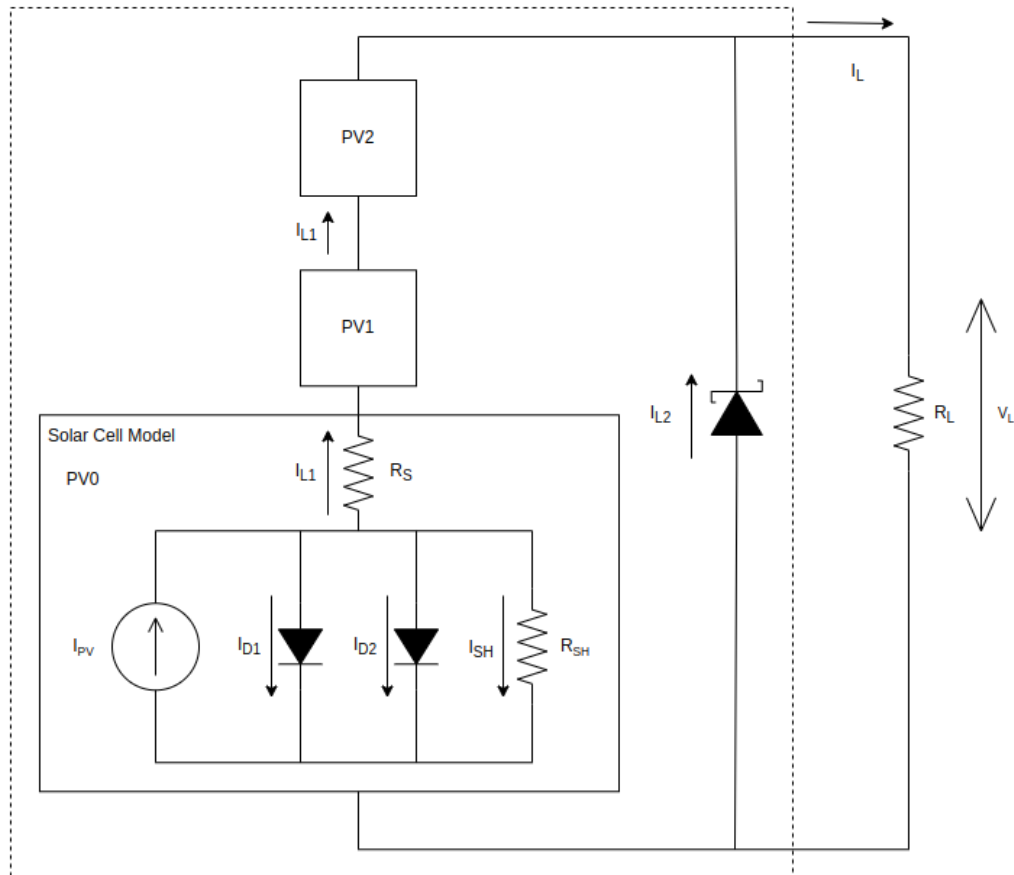## 2.2.1 Modeling Photovoltaic Strings

Figure 2.33: Solar Module Model

2.2.2 Modeling Bypass Diodes

2.2.3 Evaluation of Solar Module Models

Introduction for evaluation of solar module models.

2.2.3.1 Solar Module Test Setup

Refer to cell test setup and modifications for solar modules. Discuss applying a power supply on the input of the module.

2.2.3.2 Solar Module Dataset

1. Discussion of modules assembled, individual cell I-V curves

2. Discussion of lamination process (add reference to appendix for full procedure) and expected effect on efficiency

2.2.3.3 Modeling Solar Module Datasets

Compare Python model using extracted parameters against module I-V curves.

2.2.3.4 Results

Holistic evaluation w/ table on statistics of model: e.g. for the model and extracted module parameters, what is the overall module accuracy and precision?

2.3 Modeling Solar Arrays

Finally, we take the solar module model developed in the previous section and combine it with many other modules in series to form a solar array model. In this section we will focus on the global I-V curve generated from the solar array, and how the overall properties of the curve change under differing environmental conditions, namely irradiance changes and partial shading. We'll also look at the temporal properties of a solar array model, such as how long it takes to effectively change voltage across the solar array.

2.3.1 Modeling Shading Effects

2.3.2 Modeling Dynamic Behaviors

2.3.3 Evaluation of Solar Array Models

Introduction for evaluation of solar array models.

2.3.3.1 Solar Array Test Setup

Discuss outside array testing.

2.3.3.2 Modeling Solar Array Datasets

Compare Python model using extracted parameters against array I-V curves.

2.3.3.3 Results

Holistic evaluation w/ table on statistics of model: e.g. for the model and extracted array parameters, what is the overall array accuracy and precision?

2.4 Conclusion

Insert conclusion on chapter topics and results.

Chapter 3

Optimizing Photovoltaics

In this chapter, **Optimizing Photovoltaics**, we use the models generated from the previous chapter to generate potential solar array designs for the solar vehicle. Along the way, we propose various statistical methods and algorithms such as hierarchy clustering and compatibility matching to pick cells for module assembly. This allows us to develop heuristics to minimize mismatch effects discussed in section 2.2. We also run cost-benefit analyses of module sizes versus bypass diodes types to determine the ideal module size for specific areas of the solar vehicle, which may experience various amounts of shading over time. Finally, we propose two array designs: one with these optimizations and one without (based off of our historical processes), and attempt to estimate the cost and efficiency savings attributable to each optimization.

3.1 Solar Cell Matching

3.2 Solar Module Sizing

3.3 Solar Array Design

3.4 Conclusion

Insert conclusion on chapter topics and results.

Chapter 4

Optimizing Photovoltaic Systems

In this final chapter, **Optimizing Photovoltaic Systems**, we explore the surrounding infrastructure around the solar array that enables it to operate at its full potential. In particular, we take a look at the maximum power point tracking (MPPT) hardware (HW) used to control the solar array and propose a suite of MPPT algorithms that can address nonidealities in the I-V curve that were observed in section 2.3 such as global and local maximum power points (MPPs) and partial shading effects. We present a comprehensive PV system simulator that incorporates the models discussed in chapter 2 and the high level design developed in chapter 3 to evaluate the effects of these MPPT algorithms in terms of stability, convergence speed, total efficiency, and so forth. Finally, we implement a set of performant algorithms in real HW and validate that the optimizations and models perform as expected.

4.1   Energy Conversion Process

4.2   Maximum Power Point Trackers

4.3   Photovoltaic System Simulation

4.4   Simulation Results

4.5   Photovoltaic System Implementation

4.6   Real World Results

1. Discuss process of energy conversion, losses at each step, build sankey diagram

2. Introduce MPPT, MPPT algorithms

   - General theory, objective for MPPTs
   - Heuristics for solving constrained, multimodal surface optimization problems
   - Briefly discuss prior art
     - Esram et Chapman, Comparison of Photovoltaic Array Maximum Power Point Tracking Techniques
     - Hill climbing algorithms
   - Focus on interesting variations and novel techniques
     - Hill climbing algorithms - sublocal stride algorithms (Fixed, Optimal, Adaptive, Bisection stride)
     - Divide and conquer algorithms
       * Ternary search
       * Golden section search
       * Bisection method search
     - Metaheuristic optimization algorithms
       * Simulated annealing
       * Particle swarm optimization
     - Other algorithms
       * Voltage sweep
       * Fuzzy logic controllers
       * Newton-Raphson method
       * Trapezium method
       * Artificial neural networks
   - Issues with 'local' and 'global' algorithms
   - Propose a multi-hierarchical MPPT algorithm framework
     - Optimizing goals for each part of the hierarchy
     - Proposed clusterings of algorithms

4. Present a model for DC-DC converter and how it works in relation to an MPPT (bridge HW to SW)

5. Present system simulator

   - Environmental modeling
   - Array modeling
   - MPPT algorithm modeling

6. Simulator results

   - Impulse response (look at steady state behavior)
   - Step response (look at convergence speed, steady state behavior)
   - Simulated environmental profile response
   - Efficiency analysis and metrics, figure of merit

7. Introduce MPPT HW and how MPPT algorithms were implemented in HW (likely move to Appendix)

8. Real world testing results

Reset sankey with real data

4.7 Conclusion

Insert conclusion on chapter topics and results.
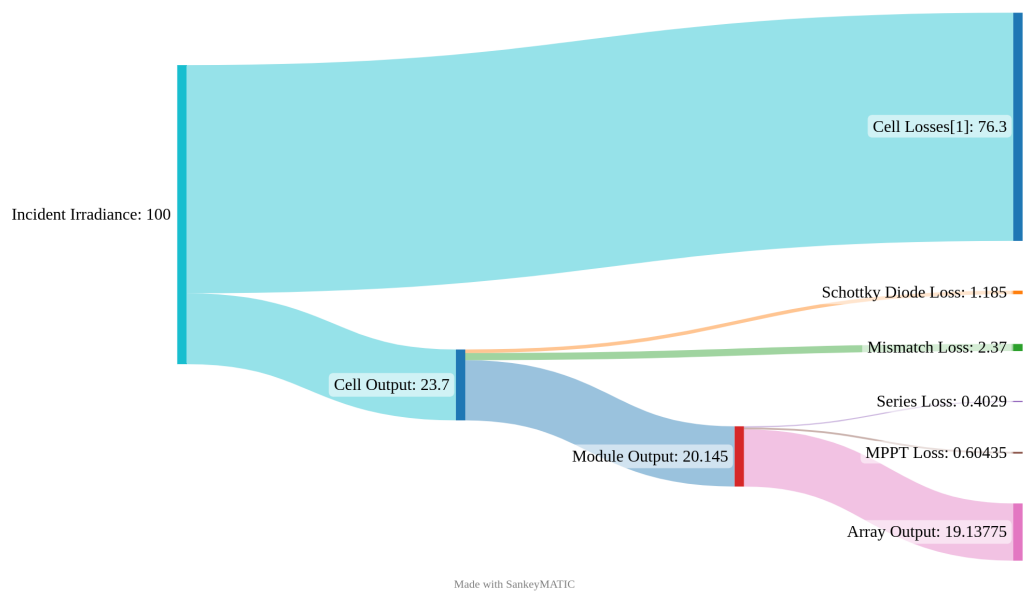
Figure 4.1: Sankey Diagram for Photovoltaic System

Chapter 5

Conclusion

Bibliography

[1]   Alaa Y. Al-Ahmad et al. "An Economic LED Solar Simulator Design".
        In: *IEEE Journal of Photovoltaics* 12.2 (2022), pp. 521–525. DOI: 10.
        1109/JPHOTOV.2022.3143460.

[2]   Mirza Qutab Baig, Hassan Abbas Khan, and Syed Muhammad Ahsan.
        "Evaluation of solar module equivalent models under real operating
        conditions—A review". In: *Journal of Renewable and Sustainable En-
        ergy* 12.1 (2020), p. 012701. DOI: 10.1063/1.5099557. eprint: https:
        //doi.org/10.1063/1.5099557. URL: https://doi.org/10.1063/
        1.5099557.

[3]   S. Bowden and A. Rohatgi. "Rapid and Accurate Determination of Se-
        ries Resistance and Fill Factor Losses in Industrial Silicon Solar Cells".
        In: *17th European Photovoltaic Solar Energy Conference*. Munich, Ger-
        many, 22/10/2001 2001.

[4]   M. Chegaar et al. "Effect of Illumination Intensity on Solar Cells Pa-
        rameters". In: *Energy Procedia* 36 (2013). TerraGreen 13 International
        Conference 2013 - Advancements in Renewable Energy and Clean En-
        vironment, pp. 722–729. ISSN: 1876-6102. DOI: https://doi.org/10.
        1016/j.egypro.2013.07.084. URL: https://www.sciencedirect.
        com/science/article/pii/S1876610213011703.

[5]   Javier Cubas, Santiago Pindado, and Carlos Manuel. "Explicit Expres-
        sions for Solar Panel Equivalent Circuit Parameters Based on Analyt-
        ical Formulation and the Lambert W-Function". In: *Energies* 7 (June
        2014), pp. 4098–4115. DOI: 10.3390/en7074098.

[6]   Javier Cubas, Santiago Pindado, and Marta Victoria. "On the analyt-
        ical approach for modeling photovoltaic systems behavior". In: *Jour-
        nal of Power Sources* 247 (2014), pp. 467–474. ISSN: 0378-7753. DOI:

https://doi.org/10.1016/j.jpowsour.2013.09.008. URL: https://www.sciencedirect.com/science/article/pii/S0378775313014997.

[7] D.M. Fébba et al. "Impacts of temperature and irradiance on polycrystalline silicon solar cells parameters". In: *Solar Energy* 174 (2018), pp. 628–639. ISSN: 0038-092X. DOI: https://doi.org/10.1016/j.solener.2018.09.051. URL: https://www.sciencedirect.com/science/article/pii/S0038092X18309435.

[8] *First long-range solar EV Lightyear One will run on SunPower Maxeon technology*. en-US. Sunpower. Dec. 2019. URL: https://sunpower.maxeon.com/int/blog/lightyear-one-will-run-sunpower-maxeon-technology.

[9] *Fixure Uniformity and How to Measure It*. en-US. Hortilux. URL: https://eyehortilux.com/grow-lighting-guide/systems/fixture-uniformity-and-efficiency/.

[10] R.N. Hall. "Silicon photovoltaic cells". In: *Solid-State Electronics* 24.7 (1981), pp. 595–616. ISSN: 0038-1101. DOI: https://doi.org/10.1016/0038-1101(81)90188-X. URL: https://www.sciencedirect.com/science/article/pii/003811018190188X.

[11] Yoshihiro Hishikawa et al. "Temperature dependence of the short circuit current and spectral responsivity of various kinds of crystalline silicon photovoltaic devices". In: *Japanese Journal of Applied Physics* 57.8S3 (July 2018), 08RG17. DOI: 10.7567/JJAP.57.08RG17. URL: https://dx.doi.org/10.7567/JJAP.57.08RG17.

[12] *History*. en-US. Sunpower. 2022. URL: https://us.sunpower.com/company/history.

[13] *Ideality factor*. PVEducation. URL: https://www.pveducation.org/pvcdrom/solar-cell-operation/ideality-factor#:~:text=The%20ideality%20factor%20of%20a,certain%20assumptions%20about%20the%20cell.

[14] Amit Jain and Avinashi Kapoor. "A new method to determine the diode ideality factor of real solar cell using Lambert W-function". In: *Solar Energy Materials and Solar Cells* 85.3 (2005), pp. 391–396. ISSN: 0927-0248. DOI: https://doi.org/10.1016/j.solmat.2004.05.022. URL: https://www.sciencedirect.com/science/article/pii/S0927024804002442.

[15] Vandana Khanna et al. "A three diode model for industrial solar cells and estimation of solar cell parameters using PSO algorithm". In: *Renewable Energy* 78 (2015), pp. 105–113. ISSN: 0960-1481. DOI: https://doi.org/10.1016/j.renene.2014.12.072. URL: https://www.sciencedirect.com/science/article/pii/S0960148115000063.

[16] Eduardo López-Fraguas, José M. Sánchez-Pena, and Ricardo Vergaz. "A Low-Cost LED-Based Solar Simulator". In: *IEEE Transactions on Instrumentation and Measurement* 68.12 (2019), pp. 4913–4923. DOI: 10.1109/TIM.2019.2899513.

[17] Sara M. MacAlpine and Michael J. Brandemuehl. "Photovoltaic module model accuracy at varying light levels and its effect on predicted annual energy output". In: *2011 37th IEEE Photovoltaic Specialists Conference*. 2011, pp. 002894–002899. DOI: 10.1109/PVSC.2011.6186551.

[18] Gaetan Masson et al. *Snapshot of Global PV Markets 2022 Task 1 Strategic PV Analysis and Outreach PVPS*. Apr. 2022. ISBN: 978-3-907281-31-4.

[19] Gaetan Masson et al. *Trends in Photovoltaic Applications 2022*. Oct. 2022. ISBN: 978-3-907281-35-2.

[20] *Measurement of Series Resistance*. PVEducation. URL: https://www.pveducation.org/pvcdrom/characterisation/measurement-of-series-resistance.

[21] Peter R. Michael, Danvers E. Johnston, and Wilfrido Moreno. "A conversion guide: solar irradiance and lux illuminance". In: *Journal of Measurements in Engineering* 8.4 (Dec. 2020), pp. 153–166. DOI: 10.21595/jme.2020.21667. URL: https://doi.org/10.21595/jme.2020.21667.

[22] Vasiliki Naskari et al. "Design and implementation of an indoors light simulator". In: (2022), pp. 1–6. DOI: 10.1109/SEEDA-CECNSM57760.2022.9932899.

[23] Jenny Nelson. "Introduction". In: *The physics of Solar Cells*. Imperial College Press, 2013, p. 14.

[24] *Net Zero by 2050*. Paris: IEA Photovoltaic Power Systems Programme, 2021.

[25]   Foteini Plyta, Thomas R. Betts, and Ralph Gottschalg. "Potential for LED solar simulators". In: (2013), pp. 0701–0705. DOI: 10.1109/PVSC.2013.6744248.

[26]   United Nations Environment Programme. *Paris Agreement.* 12/12/2015. URL: https://wedocs.unep.org/20.500.11822/20830.

[27]   Bonie Johana Restrepo-Cuestas et al. "Analysis of Electrical Models for Photovoltaic Cells under Uniform and Partial Shading Conditions". In: *Computation* 10.7 (2022). ISSN: 2079-3197. DOI: 10.3390/computation10070111. URL: https://www.mdpi.com/2079-3197/10/7/111.

[28]   Dani Rusirawan and István Farkas. "Identification of Model Parameters of the Photovoltaic Solar Cells". In: *Energy Procedia* 57 (2014). 2013 ISES Solar World Congress, pp. 39–46. ISSN: 1876-6102. DOI: https://doi.org/10.1016/j.egypro.2014.10.006. URL: https://www.sciencedirect.com/science/article/pii/S1876610214013733.

[29]   David D. Smith et al. "SunPower's Maxeon Gen III solar cell: High efficiency and energy yield". In: (June 2013), pp. 0908–0913. ISSN: 0160-8371. DOI: 10.1109/PVSC.2013.6744291.

[30]   *Solar is in Production with Maxeon Solar Cells.* en-US. Aptera Motors. Oct. 2022. URL: https://aptera.us/solar-production-with-maxeon/.

[31]   Brady Tyra et al. *Electric Power Monthly.* U.S. Energy Information Administration, Oct. 2022. URL: https://www.eia.gov/electricity/monthly/archive/october2022.pdf.

Appendices

Appendix A

Acronyms and Abbreviations

BPS battery protection system

CAN controller area network

CLI command line interface

CLT central limit theorem

DC-DC direct current to direct current

DRM Direct-Reverse Model

EIA U.S. Energy Information Administration

GUI graphical user interface

GW Gigawatts

HW hardware

IEA International Energy Association

I-V current-voltage

LHRs Longhorn Racing Solar

MOSFET metal-oxide-semiconductor field-effect transistor

MPPT maximum power point tracking

MPP maximum power point

PCB printed circuit board

PPFD photosynthetic photon flux density

PV photovoltaic

P-V power-voltage

SW software

STC standard test conditions

UN United Nations

USB universal serial bus

Appendix B

Mathematical Nomenclature

A area

$b_S(E)$ spectral photon flux density

E energy

E_G bandgap

$E_{G,ref}$ reference bandgap at STC

G irradiance

G_{ref} reference irradiance at STC

I_L load current

I_D dark current, or diode current

I_{D1} carrier recombination dark current

I_{D2} surface recombination dark current

I_{PV} photocurrent, or light generated current

I_{SC} short circuit current

$I_{SC,ref}$ reference short circuit current at STC

I_{SH} shunt current

I_0 dark saturation current, or reverse saturation current

$I_{0,ref}$ reference dark saturation current at STC

K_B Boltzmann constant

K_E short circuit current constant

n ideality factor

n_1 ideality factor of space charge recombination

n_2 ideality factor of surface recombination

$QE(E)$ quantum efficiency

q electric charge constant

R_L load resistance

R_S series resistance

$R_{S,ref}$ reference series resistance at STC

R_{SH} shunt resistance

$R_{SH,ref}$ reference shunt resistance at STC

T_C cell temperature

$T_{C,ref}$ reference cell temperature at STC

V_L load voltage

V_T thermal voltage

V_{OC} open circuit voltage

$V_{OC,ref}$ reference open circuit voltage at STC

α short circuit current thermal coefficient

β open circuit voltage thermal coefficient

γ thermal voltage modifier coefficient

ζ series resistance thermal coefficient

η series resistance irradiance coefficient

κ shunt resistance thermal coefficient

ι shunt resistance irradiance coefficient

Appendix C

Design of a Multi-Channel LED Base Solar Simulator

- Measuring light uniformity Fixture Uniformity and How to Measure It

Appendix D

Calibrating the TSL2591 for an AM1.5 Spectra

In order to calibrate the readings from the sensor as a proxy for the real irradiance experienced by the solar cell, we need to compare it to either a known source or a reference pyrometer. Another way to interpret the readings in counts is to convert it into lux; Michael et al. [21] proposes several methodologies for determining and verifying a lx to W/m^2 conversion factor. They also propose an 'engineering rule of thumb', that $120lx = W/m^2$.

Add potential note later on about needing teflon to filter in saturation conditions - can this fixed by adjusting gain/integration time?

Reference Gacusan's, Burgt's thesis regarding designing low-cost pyranometer using TSL2591 and TSL2591-like sensors

- Calibrating TSL2591

    - Developing a custom lux equation
    - TSL2591 datasheet
    - Adafruit TSL2591 irradiance measurement forum thread
    - Adafruit TSL2591 lux measurement github thread
    - Irradiance and lux conversion guide

- Designing a low cost pyranometer

    - Designing a low-cost autonomous pyranometer - Burgt

- A distributed real-time short-term solar irradiation forecasting network for photovoltaic systems - Gacusan

- A low-cost system for real-time measuring of the sunlight incident angle using IoT - Botero-Valencia et al

- A low-cost luxometer benchmark for solar illuminance measurement system based on the internet of things - Lorenzo et al

-

Appendix E

Curve Tracer Design

Appendix F

Blackbody Design

TODOS

79